JM PAPERS

Study of the linear models in estimating coherent velocity and temperature structures for compressible turbulent channel flows

Xianliang Chen[1], Cheng Cheng[2], Jianping Gan[1] and Lin Fu[1,2,3],†

[1]Department of Mathematics and Center for Ocean Research in Hong Kong and Macau (CORE), The Hong Kong University of Science and Technology, Clear Water Bay, Kowloon, Hong Kong, PR China

[2]Department of Mechanical and Aerospace Engineering, The Hong Kong University of Science and Technology, Clear Water Bay, Kowloon, Hong Kong, PR China

[3]HKUST Shenzhen-Hong Kong Collaborative Innovation Research Institute, Futian, Shenzhen, PR China

Linear models, based on stochastically forced linearized equations, are deployed for spectral linear stochastic estimation (SLSE) of the velocity and temperature fluctuations in compressible turbulent channel flows with a bulk Mach number of 1.5. Through comparison with the direct numerical simulation (DNS) data, an eddy-viscosity-enhanced model (eLNS) outperforms the one not enhanced (LNS) in computing the coherence and amplitude ratio of streamwise velocity at different wall-normal heights, but they both largely deviate from DNS regarding the temperature prediction. For further investigation, the eigenspectra and pseudospectra of the linear operators are scrutinized. The eddy viscosity is shown to stabilize the eigenmodes and decrease the non-normality of the vortical modes. Consequently, the relative importance of acoustic and entropy modes increases, and they can contribute 20 % to 55 % of the response growth, which is not supported by DNS. Hence, it is an intrinsic defect of the eLNS model introduced by turbulence modelling. After a procedure of cospectrum decomposition, the contributions of acoustic and entropy components are filtered out. The resulting SLSE quantities for velocity, temperature and their coupling are basically agreeable with DNS, demonstrating that the coherent temperature fluctuation is dominated by advection and other vortical motions, instead of the compressibility effects. Moreover, a parameter study of Reynolds and Mach numbers (from 0.3 to 4) is conducted. The semi-local units are shown to well collapse the velocity SLSE quantities to the incompressible case for streamwise-elongated structures of high coherence.

† Email address for correspondence: linfu@ust.hk

1. Introduction

Understanding and modelling compressible turbulent flows are fundamentally significant for aerodynamic applications (Bradshaw 1977). Turbulent boundary layers strongly affect the surface drag and heat transfer, so accurate predictive models are important for reliable vehicle design and flow control (Gatski & Bonnet 2013). Compared with the incompressible one, additional thermodynamic processes are present in high-speed turbulent flows, such as heat transfer, acoustic fluctuations, dilatational work and high-enthalpy effects (Di Renzo, Fu & Urzay 2020; Di Renzo & Urzay 2021; Fu *et al.* 2021; Fu, Bose & Moin 2022). Due to the theoretical complexity and practical significance, compressible wall-bounded turbulence has become a hot topic.

The mean flow properties of compressible turbulence have been extensively studied. The hypothesis of Morkovin (1962) is widely verified, stating that at moderate free stream Mach numbers ($Ma_\infty \lesssim 5$), the dilatation effect is small, and any differences from incompressible turbulence can be accounted for by mean variations of fluid properties (Coleman, Kim & Moser 1995; Pirozzoli, Grasso & Gatski 2004; Duan, Beekman & Martin 2010). Lagha *et al.* (2011) even show that the hypothesis is applicable with Ma_∞ up to 20 for flat-plate boundary layers. Thereby, velocity transformation can be designed using only the mean flow. The transformed streamwise velocity profile can match the incompressible one within and below the logarithmic region with very high accuracy (van Driest 1951; Trettel & Larsson 2016; Griffin, Fu & Moin 2021; Bai, Griffin & Fu 2022). Meanwhile, the mean temperature is shown to be nearly a quadratic function of the mean velocity (Walz 1969; Duan & Martín 2011; Zhang *et al.* 2014). Strong Reynolds analogy (SRA) and its extensions are proposed, connecting the temperature and velocity fluctuations (Morkovin 1962; Huang, Coleman & Bradshaw 1995; Zhang *et al.* 2014). In a recent work, Cheng & Fu (2023*a*) note that the profile of turbulent Prandtl number Pr_t in supersonic channels is very close to the incompressible case with heat transfer (Antonia, Abe & Kawamura 2009). They suggest that the coherent temperature fluctuations behave like a passive scalar, and the coupling between the velocity and temperature fields results largely from the advection effect.

In addition to the mean flow, much progress has been made in understanding the structures of velocity and temperature fluctuations, owing to the advancement of experimental and numerical techniques, especially the direct numerical simulation (DNS, Moin & Mahesh 1998). In the near-wall region, small-scale temperature streaks are observed elongated in the streamwise direction, analogous to the streamwise velocity streaks (Coleman *et al.* 1995; Duan *et al.* 2010). The spanwise spacing of streaks is shown to decrease with rising *Ma* on adiabatic walls, and increase by wall cooling; it experiences much less variation if expressed in semi-local units (Morinishi, Tamano & Nakabayashi 2004). Within and above the logarithmic layer, energy-containing large-scale and very-large-scale motions (LSMs and VLSMs), as first reported in incompressible flows (Kim & Adrian 1999), are identified in supersonic boundary layers experimentally (Ganapathisubramani, Clemens & Dolling 2006; Bross, Scharnowski & Kähler 2021) and numerically (Ringuette, Wu & Martín 2008; Huang, Duan & Choudhari 2022). Unlike the near-wall motions, the characteristic scales of LSMs and VLSMs are not very sensitive to compressibility effects (Pirozzoli, Bernardini & Grasso 2008; Williams *et al.* 2018; Cheng & Fu 2022*b*). The LSMs populating the logarithmic and outer regions are

known to exert footprints, i.e. have effects of velocity modulation and superposition, on the near-wall motions (Abe, Kawamura & Choi 2004; Hutchins & Marusic 2007), which is the basis of the inner–outer interaction model (IOIM, Marusic, Mathis & Hutchins 2010). Using the DNS of supersonic boundary layers, Bernardini & Pirozzoli (2011) and Pirozzoli & Bernardini (2011) demonstrate that the temperature fluctuations also experience inner–outer interaction, though the modulation effect seems weaker than the velocity. Yu & Xu (2022) extend IOIM to realize a predictive model for both velocity and temperature fields in compressible boundary layers, considering the modified SRA and the superposition and modulation from LSMs. Meanwhile, the inner–outer interaction of temperature fluctuations indicates that they can also be regarded as a wall-attached quantity, hence described by the well-known attached-eddy model (AEM, Townsend 1976). This is supported by accumulating evidence concerning the geometrical self-similarity of temperature in the logarithmic region (Cheng & Fu 2022*b*; Yu *et al.* 2022; Chen *et al.* 2023). Moreover, Cheng & Fu (2023*a*) point out that in the logarithmic region, only the scales corresponding to the attached eddies and VLSMs are firmly coupled; the Reynolds number *Re* acts as the crucial similarity parameter in constructing the coupling, rather than the Mach number.

To estimate and model coherent large-scale structures, the spectral linear stochastic estimation (SLSE) approach is helpful. SLSE originates from the extensively used stochastic estimation (Adrian 1979; Adrian & Moin 1988), which can provide an estimated velocity signal given a measurement at another point from experiments or simulations. Considering the multi-scale feature of turbulence, SLSE is performed in the Fourier space, which takes advantage of the coherence of large-scale structures and suppresses small-scale random noise (Tinney *et al.* 2006; Baars, Hutchins & Marusic 2016). A kernel function H_L is designed to relate the Fourier components at different wall-normal heights, based on the linear coherence spectrum (LCS). Over the years, SLSE has been widely deployed to study the multi-scale structures in incompressible flows and to help understand and improve AEM and IOIM (Baars, Hutchins & Marusic 2017; Encinar & Jiménez 2019; Cheng & Fu 2022*a*, 2023*b*; Cheng, Shyy & Fu 2022). Nevertheless, its application in compressible flows is still limited. Very recently, Cheng & Fu (2022*b*, 2023*a*) extend the SLSE framework for compressible flows. The self-similarity of thermodynamic quantities and the coupling effects between velocity and temperature are thus investigated. This extended SLSE framework is considered in this work for compressible channel flows.

By definition, the LCS and H_L in SLSE involve ensemble-averaged cospectra, so their calculation requires a series of instantaneous measurements or numerical data, which are more challenging to obtain than the mean flow. In an alternative method, Madhusudanan, Illingworth & Marusic (2019) obtain H_L using the linearized incompressible Navier–Stokes (NS) equations, which requires only the mean flow as the input. Their stochastically forced, eddy-viscosity-enhanced linear model gives agreeable LCS with the DNS data, except in the near-wall region. For improvement, Gupta *et al.* (2021) model the amplitude distribution of the stochastic forcing using mean flow quantities. The resulting LCS and H_L are quite close to the DNS data, though the prediction can still struggle in the near-wall region. Notably, the linearized NS equations have long been utilized in turbulence research, as will be introduced at length later. Thereby, it is a natural thought to develop a linear model for compressible turbulent flows, so that the LCS and H_L can be obtained using only mean flow quantities. In this way, the coherence of velocity and temperature fluctuations, as well as their coupling effects, can be further investigated. Such a linear model is of particular significance for compressible flows, because the instantaneous experimental and DNS data are much more limited than the incompressible counterparts due to larger parameter space and higher facility requirements

(Gatski & Bonnet 2013). It is the objective of this work to develop a linear model for SLSE in compressible turbulent channel flows. We find that a direct extension of the incompressible model to the compressible case does not provide satisfactory SLSE results, especially for temperature fluctuations. Thereby, we will scrutinize the mathematical properties and physical relevance of different linear models, and assess carefully their behaviours.

To set more grounds for the present work, the approaches based on the linearized NS equations for turbulent flows are introduced in more detail. Early works find that the incompressible turbulent mean flow (one dimensional) is globally stable, i.e. there are no unstable modes through linear stability analysis (Malkus 1956; Reynolds & Hussain 1972). For this globally stable system, non-modal instability theory and the resolvent-based input–output analysis, first applied for laminar flows (Trefethen *et al.* 1993; Schmid & Henningson 2001), are extended to study the transient behaviour of turbulent mean flows. These linear approaches are successful in studying the multi-scale characteristic motions (del Álamo & Jiménez 2006; Hwang & Cossu 2010; Abe, Antonia & Toh 2018), constructing low-rank predictive models (McKeon & Sharma 2010; Moarref *et al.* 2013; Illingworth, Monty & Marusic 2018), designing flow control strategies (Moarref & Jovanović 2012; Ran, Zare & Jovanović 2020) and so on. Many of these works adopt the eddy-viscosity-enhanced models, where the Reynolds stress fluctuation is linearized using the eddy viscosity μ_t, to partly model the colour of the forcing. The eddy-viscosity-enhanced models are shown to perform better than those without using μ_t, especially for estimating fluctuations between different heights (Reynolds & Hussain 1972; Illingworth *et al.* 2018; Madhusudanan *et al.* 2019; Morra *et al.* 2021; Symon, Illingworth & Marusic 2021). The linearized-equation-based approaches have also been deployed for compressible turbulent flows. Alizard *et al.* (2015) perform the transient growth analysis on turbulent boundary layers with Ma_∞ up to 4. The inner and outer peak modes are identified from the energy growth curves with different spanwise wavenumbers, analogous to the incompressible cases. The former mode is related to the near-wall streaky motions, and the latter represents the outer-layer LSMs (and VLSMs). Bae, Dawson & McKeon (2020) extend the resolvent analysis to supersonic boundary layers and highlight the distinct features of the relatively supersonic region in the wavenumber space, which is not present in incompressible flows. Also, Chen *et al.* (2023) develop the linear response analyses subject to both optimal harmonic and stochastic forcing for supersonic channel flows, and analyse the response characteristics over wide ranges of *Ma* and *Re*. To model the linearized Reynolds stress and turbulent heat flux, μ_t and SRA are introduced in some of these works (Alizard *et al.* 2015; Pickering *et al.* 2021; Chen *et al.* 2023). Nevertheless, no quantitative comparisons have been made with DNS or experiments in these works, so the accuracy of these linear models remains unclarified. It is also a task of the present work to make such a quantitative assessment regarding SLSE using the DNS database constructed in the present authors' group.

In addition, there are some theoretical issues that require to be addressed regarding the linearized equations for compressible turbulent flows. For example, the singular value of the resolvent by Bae *et al.* (2020) (their figure 1) has relatively strong oscillations when the response mode is relatively supersonic. Madhusudanan & McKeon (2022) (and also our own experience) note that relatively supersonic modes have amplified acoustic components in the free stream, and the results can be dependent on the height of the computational domain (which is artificially selected) for boundary layers. These facts suggest that there can be some fundamental differences in the linear models between incompressible and compressible flows, in addition to the widely addressed similarities. However, the differences have not been fully resolved. Also, in deriving the compressible
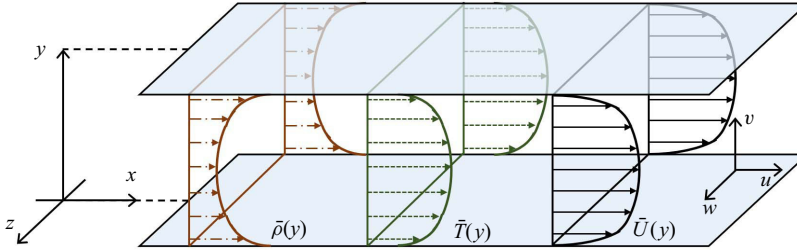
Figure 1. Schematic and coordinate set-up for the compressible channel flow.

eddy-viscosity-enhanced models, multiple options are available to linearize different terms, leading to numerous combinations. They deserve a careful discussion through inter-model comparisons.

The primary attention of this work is on the following three aspects, which are also its value. First, we carefully discuss the derivation and mathematical properties of the linearized equations for compressible turbulent flows, which is instructive for interpreting subsequent results (§§ 2–4). Second, we utilize the linear model to perform SLSE for streamwise velocity, temperature, and their coupling, aiming to predict the coherent velocity and temperature fluctuations based on the measurement at outer locations. Direct comparison with DNS is conducted to assess their behaviours (§ 5). Third, we discuss the physics inferred from SLSE results, especially for temperature, and conduct a parameter study to see the effects of Reynolds and Mach numbers (§§ 5 and 6). Some remarks are provided on the scope of this work. For incompressible flows, many linear models have been developed to provide continuously improved results approaching the DNS and experimental data (see the references above). These models have different treatments in linearizing the Reynolds stress, modelling the forcing, utilizing or not instantaneous DNS data and so on. Consequently, it is nearly impossible for the present work to extend and compare among all these models, especially considering the still larger parameter space in compressible flows. Thereby, we hope that the linear model in this work is both simple and instructive. Some possible extensions and future works are discussed in §§ 7 and 8.

2. Governing equations and dataset

2.1. *Compressible Navier–Stokes equations*

The canonical compressible turbulent channel flow is considered, as illustrated in figure 1. Assuming a calorically perfect gas, the governing NS equations are

$$\frac{\partial \rho}{\partial t} + \nabla \cdot (\rho \boldsymbol{u}) = 0, \tag{2.1a}$$

$$\rho \left(\frac{\partial \boldsymbol{u}}{\partial t} + \boldsymbol{u} \cdot \nabla \boldsymbol{u} \right) = -\nabla p + \nabla \cdot \left[\mu (\nabla \boldsymbol{u} + \nabla \boldsymbol{u}^{\mathrm{T}}) \right] - \frac{2}{3} \nabla (\mu \nabla \cdot \boldsymbol{u}), \tag{2.1b}$$

$$\rho c_p \left(\frac{\partial T}{\partial t} + \boldsymbol{u} \cdot \nabla T \right) - \left(\frac{\partial p}{\partial t} + \boldsymbol{u} \cdot \nabla p \right) = \mu \left[\nabla \boldsymbol{u} : (\nabla \boldsymbol{u} + \nabla \boldsymbol{u}^{\mathrm{T}}) - \frac{2}{3} (\nabla \cdot \boldsymbol{u})^2 \right]$$
$$+ \nabla \cdot (\kappa \nabla T), \tag{2.1c}$$

where ρ, $\boldsymbol{u} = [u, v, w]^{\mathrm{T}}$, T and $p = \rho R T$ are the fluid density, velocity, temperature and pressure, respectively; R and c_p are the gas constant and isobaric specific heat; and μ and

κ are the molecular viscosity and thermal conductivity. Characteristic non-dimensional parameters are the Mach, Reynolds, Prandtl and Eckert numbers,

$$Ma_b = \frac{U_b}{a_w}, \quad Re_b = \frac{\rho_b U_b h}{\mu_w}, \quad Pr = \frac{\mu c_p}{\kappa} = 0.72, \quad Ec = \frac{U_b^2}{c_p T_w} = (\gamma_0 - 1)Ma_b^2,$$

(2.2a–d)

where the subscript w denotes quantities at the wall ($y = 0, 2h$) and h is the channel half-height. The speed of sound is $a = (\gamma_0 RT)^{1/2}$ with a constant specific heat ratio $\gamma_0 = c_p/c_v = 1.4$. The subscript 0 here is to distinguish from the LCS notation in § 2.3. The bulk density ρ_b and bulk velocity U_b are defined as $\rho_b = \int_0^{2h} \bar{\rho} \, dy/(2h)$ and $\rho_b U_b = \int_0^{2h} \overline{\rho u} \, dy/(2h)$, where the overbar denotes mean variables. The viscosity is calculated through Sutherland's law, where the fitting constant is 110.4 K and the reference temperature is 293.15 K. No-slip and isothermal walls are set on both sides as the boundary condition.

The basic variable set in (2.1) is $q = [\rho, u, v, w, T]^T$. Both the Reynolds average ($\bar{\varphi}$ with φ a time-dependent variable) and Favre average ($\tilde{\varphi} = \overline{\rho\varphi}/\bar{\rho}, \varphi \neq \rho$) are deployed. The resulting two fluctuations are denoted as φ' and φ'', respectively. For wall-bounded turbulence, it is common to use wall viscous units with a superscript +, as $x^+ = x/\delta_v$, $\rho^+ = \rho/\rho_w, u^+ = u/u_\tau$ and $T^+ = T/T_\tau$. Here the viscous length unit is $\delta_v = \mu_w/(\rho_w u_\tau)$, the friction velocity and temperature are $u_\tau = (\tau_w/\rho_w)^{1/2}$ and $T_\tau = Q_w/(\rho_w c_p u_\tau)$, where τ_w and Q_w are the wall mean shear and heat flux. The friction Reynolds number is $Re_\tau = h/\delta_v$. Furthermore, semi-local units are adopted, expressed with a superscript $*$ as $u_\tau^* = (\tau_w/\bar{\rho})^{1/2}$, $\delta_v^* = \bar{\mu}/(\bar{\rho}u_\tau^*)$, so $y^* = y/\delta_v^*$ and $Re_\tau^* = h/\delta_v^*$.

2.2. *DNS dataset and mean flow calculation*

A series of DNSs for compressible turbulent channel flows has been conducted by the present authors, as reported at length (Cheng & Fu 2022b). The calculations adopt two Ma_b of 0.8 and 1.5, and cover a Re_b range of 7667–20 020 ($Re_\tau = 436$–1150). The domains are all rectangular, in the same sizes $L_x \times L_z \times L_y = 4\pi h \times 2\pi h \times 2h$. Previous studies have verified that this set-up can capture most of the large-scale motions in the outer region (Agostini & Leschziner 2014). Readers can refer to Cheng & Fu (2022b, 2023a) for more analyses on the DNS statistics. The case $Ma_b = 1.5$, $Re_b = 20\,020$ ($Re_\tau = 1150$, $Re_\tau^* = 780$) is selected as the benchmark case for this study, which is of the highest Ma_b and Re in our dataset. The valuable DNS data allow a quantitative evaluation of the linear model results.

In addition to DNS, well-established universal relations can be used to obtain efficiently the turbulent mean flows, by solving a set of ordinary differential equations (ODEs) (Griffin, Fu & Moin 2022, 2023; Chen *et al.* 2023; Song, Zhang & Xia 2023). The ODE-based method of Chen *et al.* (2023) is used here, which requires only the values of Ma_b and Re_b as the input. We will demonstrate in § 6 that the ODE-based mean flow can be used in the linear models for SLSE, which will serve the parameter study.

2.3. *Spectral linear stochastic estimation*

As motivated in § 1, SLSE predicts the coherent portion of fluctuations at different heights as a reflection of the superposition effects. For consistency with the equations in § 3.1, the SLSE quantities are defined based on the Favre average. As the mean flow is homogeneous

in the wall-parallel directions, Fourier decomposition is applied on q'' as

$$q''(x, y, z, t) = \iint_{-\infty}^{\infty} \hat{q}''(y, t; k_x, k_z) \exp[i(k_x x + k_z z)] \, dk_x \, dk_z, \tag{2.3}$$

where k_x and k_z are the streamwise and spanwise wavenumbers, and $\hat{q}''$ is the shape function. In SLSE, the spectral signals $\hat{u}''$ between the locations of measurement y_m and prediction y_p are connected through a complex-valued kernel function H_L (Tinney *et al.* 2006),

$$\left.\begin{aligned}
\hat{u}_p''(y_p, t; k_x, k_z) &= H_{L,uu}(y_p, y_m; k_x, k_z)\hat{u}''(y_m, t; k_x, k_z), \\
H_{L,uu}(y_p, y_m; k_x, k_z) &= \frac{\langle \hat{u}''(y_p, t; k_x, k_z)\hat{u}''^{\dagger}(y_m, t; k_x, k_z)\rangle}{\langle \hat{u}''(y_m, t; k_x, k_z)\hat{u}''^{\dagger}(y_m, t; k_x, k_z)\rangle},
\end{aligned}\right\} \tag{2.4a}$$

where $\langle \cdot \rangle$ stands for ensemble average and superscript $\dagger$ denotes the complex conjugate. If the time-independent $H_{L,uu}$ is obtained, then $\hat{u}''(y_p, t; k_x, k_z)$ and $u''(x, y_p, z, t)$ at y_p can be estimated (u_p'' or $\hat{u}_p''$) given an instantaneous field (u'' or $\hat{u}''$) at y_m considering all coherent motions (Baars *et al.* 2016). In the following, k_x and k_z in the brackets will be omitted if there is no ambiguity. It is worth mentioning that $H_{L,uu}$ for compressible flows is defined differently among the literature. The u'' in (2.4a) can be replaced with u' or other density-weighting forms. Cheng & Fu (2022b) show that different density-weighting approaches do not alter the energy distribution among scales for the benchmark case here. Also, with or without density weighting negligibly affects the streamwise and spanwise length scales of the pre-multiplied spectra peaks. Therefore, the definition in (2.4a) is used throughout. Similar to that for u'', SLSE can be deployed to estimate $T''(y_p)$ given $T''(y_m)$ or $u''(y_m)$. The latter combination concerns the coupling effects between u'' and T'' (Cheng & Fu 2023a). The two kernel functions are defined as

$$H_{L,TT}(y_p, y_m) = \frac{\langle \hat{T}''(y_p, t)\hat{T}''^{\dagger}(y_m, t)\rangle}{\langle \hat{T}''(y_m, t)\hat{T}''^{\dagger}(y_m, t)\rangle}, \quad H_{L,uT}(y_p, y_m) = \frac{\langle \hat{T}''(y_p, t)\hat{u}''^{\dagger}(y_m, t)\rangle}{\langle \hat{u}''(y_m, t)\hat{u}''^{\dagger}(y_m, t)\rangle}. \tag{2.4b}$$

Following Tinney *et al.* (2006), the amplitude of $H_{L,uu}$ (also for $H_{L,TT}, H_{L,uT}$) is further decomposed into two parts, as

$$|H_{L,uu}(y_p, y_m)|^2 = A_{pm,uu}^2(y_p, y_m)\gamma_{uu}^2(y_p, y_m), \tag{2.5}$$

where $A_{pm}(y_p, y_m; k_x, k_z)$ measures the fluctuation amplitude ratio at a specific length scale, and $\gamma^2(y_p, y_m; k_x, k_z)$ is the 2-D LCS; their expressions are

$$A_{pm,uu}(y_p, y_m) = \sqrt{\frac{\langle |\hat{u}''(y_p)|^2\rangle}{\langle |\hat{u}''(y_m)|^2\rangle}}, \quad \gamma_{uu}^2(y_p, y_m) = \frac{|\langle \hat{u}''(y_p, t)\hat{u}''^{\dagger}(y_m, t)\rangle|^2}{\langle |\hat{u}''(y_p, t)|^2\rangle\langle |\hat{u}''(y_m, t)|^2\rangle}. \tag{2.6a}$$

The denominator of γ_{uu}^2 comprises two individual 2-D energy spectra of u'' at y_p and y_m, while the numerator is the absolute value of the u'' cospectrum between the two heights. Therefore, γ_{uu}^2 reflects the maximum correlation coefficient at each Fourier scale, hence instructive for understanding structural coherence. By definition, $0 \le \gamma^2 \le 1$; $\gamma^2 = 1$ represents perfect coherence while $\gamma^2 = 0$ means no coherence. The phase of $H_{L,uu}$ is not reflected in (2.5), which also matters as a measure of the structural angle difference in

the x–z plane (Baars *et al.* 2016). Similar to (2.6*a*), γ_{TT}^2 and γ_{uT}^2 are defined as

$$\gamma_{TT}^2(y_p, y_m) = \frac{|\langle \hat{T}''(y_p, t)\hat{T}''^\dagger(y_m, t)\rangle|^2}{\langle|\hat{T}''(y_p, t)|^2\rangle\langle|\hat{T}''(y_m, t)|^2\rangle}, \quad \gamma_{uT}^2(y_p, y_m) = \frac{|\langle \hat{T}''(y_p, t)\hat{u}''^\dagger(y_m, t)\rangle|^2}{\langle|\hat{T}''(y_p, t)|^2\rangle\langle|\hat{u}''(y_m, t)|^2\rangle}. \tag{2.6b}$$

Calculating H_L, γ^2 and A_{pm}^2 requires the 2-D cospectrum of $\hat{q}''$,

$$\boldsymbol{\Phi}(y, y'; k_x, k_z) = \langle \hat{q}''(y, t; k_x, k_z)\hat{q}''^H(y', t; k_x, k_z)\rangle, \tag{2.7}$$

where H denotes the Hermite transpose. The cospectrum is computed using a time series of instantaneous measurements or numerical data. As an alternative, it can be obtained through a linear model based on the linearized (2.1), as introduced in § 1. The construction of the linear model is discussed below.

3. Linear models for compressible flows

Although the linear models in incompressible flows have been extensively addressed, their compressible counterparts deserve a careful discussion.

3.1. *Mean flow and fluctuation equations*

To establish a linear model, the governing equation for q'' is derived first. Following standard procedures, the time-averaged (2.1) is

$$\frac{\partial \bar{\rho}}{\partial t} + \tilde{u}_j \frac{\partial \bar{\rho}}{\partial x_j} + \bar{\rho} \frac{\partial \tilde{u}_j}{\partial x_j} = 0, \tag{3.1a}$$

$$\bar{\rho}\left(\frac{\partial \tilde{u}_i}{\partial t} + \tilde{u}_j \frac{\partial \tilde{u}_i}{\partial x_j}\right) = -\frac{\partial \bar{p}}{\partial x_i} + \frac{\partial \bar{\tau}_{ij}}{\partial x_j} + \frac{\partial}{\partial x_j}\underbrace{(-\bar{\rho}\widetilde{u_i''u_j''})}_{\text{Reynolds stress}}, \quad i = 1, 2, 3, \tag{3.1b}$$

$$\bar{\rho}c_v\left(\frac{\partial \tilde{T}}{\partial t} + \tilde{u}_j \frac{\partial \tilde{T}}{\partial x_j}\right) = \frac{\partial}{\partial x_j}\left(\tilde{\kappa}\frac{\partial \tilde{T}}{\partial x_j}\right) - \bar{p}\frac{\partial \tilde{u}_j}{\partial x_j} + \bar{\tau}_{ij}\frac{\partial \tilde{u}_i}{\partial x_j} + \frac{\partial}{\partial x_j}\underbrace{(-\bar{\rho}c_v\widetilde{u_j''T''})}_{\substack{\text{turbulent} \\ \text{heat flux}}}$$

$$- \underbrace{\overline{p'\frac{\partial u_j''}{\partial x_j}}}_{\substack{\text{pressure} \\ \text{dilatation}}} + \underbrace{\overline{\tau_{ij}'\frac{\partial u_i''}{\partial x_j}}}_{\substack{\text{viscous} \\ \text{dissipation}}}. \tag{3.1c}$$

Here the mean pressure is $\bar{p} = \bar{\rho}R\tilde{T}$, and the viscous stress (and also for $\tilde{\kappa}$) is approximated, following the suggestion by Gatski & Bonnet (2013), as

$$\left.\begin{array}{l} \bar{\tau}_{ij} \approx \tilde{\mu}\left(\dfrac{\partial \tilde{u}_i}{\partial x_j} + \dfrac{\partial \tilde{u}_j}{\partial x_i} - \dfrac{2}{3}\dfrac{\partial \tilde{u}_k}{\partial x_k}\delta_{ij}\right), \\[3mm] \tau_{ij}' \approx \tilde{\mu}\left(\dfrac{\partial u_i''}{\partial x_j} + \dfrac{\partial u_j''}{\partial x_i} - \dfrac{2}{3}\dfrac{\partial u_k''}{\partial x_k}\delta_{ij}\right) + \mu''\left(\dfrac{\partial \tilde{u}_i}{\partial x_j} + \dfrac{\partial \tilde{u}_j}{\partial x_i} - \dfrac{2}{3}\dfrac{\partial \tilde{u}_k}{\partial x_k}\delta_{ij}\right), \end{array}\right\} \tag{3.2}$$

where $\tilde{\mu} \approx \mu(\tilde{T})$, $\mu'' \approx (\partial\mu/\partial T)T''$, and δ_{ij} is the Kronecker delta. Equation (3.1) uses the Favre-averaged quantities, so it can be regarded as a governing equation for the mean

973 A36-8

flow $\tilde{q} = [\bar{\rho}, \tilde{u}_i, \tilde{T}]^T$, though there are unclosed terms regarding $q'' = [\rho', u_i'', T'']^T$. The physical meanings of these unclosed terms, as underbraced, have been elaborated before (e.g. Huang *et al.* 1995). In particular, the last two terms in (3.1c) are crucial for the energy transfer between the internal energy and turbulent kinetic energy $k \equiv \overline{u_j'' u_j''}/2$ (Lele 1994). For reference, the governing equation for k is provided as

$$\bar{\rho}\left(\frac{\partial k}{\partial t} + \tilde{u}_j \frac{\partial k}{\partial x_j}\right) = -\bar{\rho}\widetilde{u_i'' u_j''}\frac{\partial \tilde{u}_i}{\partial x_j} - \frac{\partial}{\partial x_j}(\bar{\rho}\widetilde{u_j'' k''} + \overline{p' u_j''} - \overline{\tau_{ij}' u_i''}) + \overline{p'\frac{\partial u_j''}{\partial x_j}} - \overline{\tau_{ij}'\frac{\partial u_i''}{\partial x_j}}. \quad (3.3)$$

The governing equations for q'' are obtained after a subtraction between (2.1) and (3.1). The fluctuating continuity equation is

$$\left(\frac{\partial \rho'}{\partial t} + \tilde{u}_j \frac{\partial \rho'}{\partial x_j}\right) + \left(\bar{\rho}\frac{\partial u_j''}{\partial x_j} + \frac{\partial \tilde{u}_j}{\partial x_j}\rho' + \frac{\partial \bar{\rho}}{\partial x_j}u_j''\right) = \underbrace{-\frac{\partial \rho' u_j''}{\partial x_j}}_{N_\rho''}. \quad (3.4a)$$

The equation is rearranged so that the terms on the left-hand side are linear terms of q'', while the one on the right-hand side is nonlinear, denoted as N_ρ''. Similarly, the fluctuating momentum equation ($i = 1, 2, 3$) takes the form of

$$\bar{\rho}\left(\frac{\partial u_i''}{\partial t} + \tilde{u}_j \frac{\partial u_i''}{\partial x_j}\right) + (\rho' \tilde{u}_j + \bar{\rho} u_j'')\frac{\partial \tilde{u}_i}{\partial x_j} + \frac{\partial p'}{\partial x_i} - \frac{\partial \tau_{ij}'}{\partial x_j}$$

$$= -\frac{\partial}{\partial x_j}\underbrace{[\bar{\rho}(u_i'' u_j'' - \widetilde{u_i'' u_j''})]}_{\text{Reynolds stress fluctuation}} - \underbrace{\left(\frac{\partial \rho' u_i''}{\partial t} + \frac{\partial \rho' u_i'' \tilde{u}_j}{\partial x_j} + \rho' u_j''\frac{\partial \tilde{u}_i}{\partial x_j}\right)}_{N_{u_i}''}. \quad (3.4b)$$

Same as (3.4a), the linear and nonlinear terms are placed on the two sides. The nonlinear terms are classified into two groups. The first group is the fluctuation of the Reynolds stress tensor, and the second group collects all the second- and higher-order terms related to ρ'. The classification in (3.4b) is not unique. For example, one can expand N_{u_i}'' using (3.4a). Different possibilities will be discussed in §7. Notably, when DNS is conducted, there is a temporarily-varying body force term in the streamwise momentum equation to fix the mass flux (e.g. Yao & Hussain 2020). This term is spatially uniform in the current DNS data, so it appears only at the scale $k_x = k_z = 0$, hence not included in (3.4b). The fluctuating internal energy equation is

$$\bar{\rho}c_v\left(\frac{\partial T''}{\partial t} + \tilde{u}_j \frac{\partial T''}{\partial x_j}\right) + c_v(\rho' \tilde{u}_j + \bar{\rho}u_j'')\frac{\partial \tilde{T}}{\partial x_j} - \frac{\partial}{\partial x_j}\left(\bar{\kappa}\frac{\partial T''}{\partial x_j} + \kappa''\frac{\partial \tilde{T}}{\partial x_j}\right)$$

$$+ \left(\bar{p}\frac{\partial u_j''}{\partial x_j} + p'\frac{\partial \tilde{u}_j}{\partial x_j}\right) - \left(\bar{\tau}_{ij}\frac{\partial u_i''}{\partial x_j} + \tau_{ij}'\frac{\partial \tilde{u}_i}{\partial x_j}\right) = -\frac{\partial}{\partial x_j}\underbrace{[\bar{\rho}c_v(u_j'' T'' - \widetilde{u_j'' T''})]}_{\substack{\text{turbulent heat flux} \\ \text{fluctuation}}}$$

$$- \underbrace{\left(p'\frac{\partial u_j''}{\partial x_j} - \overline{p'\frac{\partial u_j''}{\partial x_j}}\right)}_{\substack{\text{pressure dilatation} \\ \text{fluctuation}}} + \underbrace{\left(\tau_{ij}'\frac{\partial u_i''}{\partial x_j} - \overline{\tau_{ij}'\frac{\partial u_i''}{\partial x_j}}\right)}_{\substack{\text{dissipation rate} \\ \text{fluctuation}}} - c_v\underbrace{\left(\frac{\partial \rho' T''}{\partial t} + \frac{\partial \rho' T'' \tilde{u}_j}{\partial x_j} + \rho' u_j''\frac{\partial \tilde{T}}{\partial x_j}\right)}_{N_T''}.$$

$$(3.4c)$$

Likewise, N_T'' collects all the terms related to ρ'. There are additional terms of fluctuating turbulent heat flux, pressure dilatation and dissipation rate, as underbraced. The governing equation for $k'' \equiv (u_j'' u_j''/2 - k)$ (Huang *et al.* 1995) can be similarly derived, whose full expression is listed in Appendix A.

As seen, (3.4) is far more complicated than its incompressible counterpart for deriving a linear model. The nonlinear terms N_ρ'', N_{u_i}'' and N_T'' all result from ρ', not present in incompressible cases. The remaining four nonlinear terms are classic ones in the turbulence modelling theory.

3.2. *Modelling issues and linearization*

In general, there are two types of strategies to linearize (3.4). The first one, as adopted by Bae *et al.* (2020) and Dawson & McKeon (2020), is to collect all the second- and higher-order terms of q'', i.e. those underbraced in (3.4), into the nonlinear forcing term. The resulting form is termed the LNS equation here, written in a standard operator form as

$$\frac{\partial q''}{\partial t} = \mathcal{L}_{LNS} q'' + f_{LNS}''.$$ (3.5)

Here, the linear operator $\mathcal{L}$ is only mean flow related, and f'' collects all the nonlinear terms. For later use, the temporal derivative term is not included in $\mathcal{L}$. Notably, the expression of $\mathcal{L}_{LNS}$ is exactly the same as that in the linear stability theory for laminar flows (Mack 1984).

The second strategy is to utilize turbulence modelling relations for possible linearization of the nonlinear terms, which is the counterpart of the eddy-viscosity-enhanced model for incompressible flows. However, the extension to compressible flows is much more complicated with multiple combinations. More terms require linearization besides the Reynolds stress term, which, as will be shown later, can lead to difficulties in closing the equations. Our principle here is to avoid *ad hoc* fittings by ourselves and use only the relations from classic modelling theory, which have been widely verified.

Analogous to the incompressible case, the fluctuation of the Reynolds stress term is modelled using the linearized Boussinesq assumption,

$$-\bar{\rho}(u_i'' u_j'' - \widetilde{u_i'' u_j''}) = \mu_t \left(\frac{\partial u_i''}{\partial x_j} + \frac{\partial u_j''}{\partial x_i} - \frac{2}{3} \frac{\partial u_m''}{\partial x_m} \delta_{ij} \right) - \frac{2}{3} \bar{\rho} k'' \delta_{ij}.$$ (3.6)

The turbulent heat flux is usually modelled using the SRA. The modified version by Huang *et al.* (1995) takes the form of

$$T'' = \frac{1}{Pr_t} \frac{\partial \tilde{T}}{\partial \tilde{u}} u''.$$ (3.7)

It assumes that T'' also satisfies the mixing-length relation as u'', and hints that T'' is advection dominated since it is determined by u'' and the mean-flow gradients. Based on (3.7), there are two means to linearize the turbulent heat flux term. The first one is to follow the Reynolds-averaged NS (RANS) modelling, e.g. the k–ω model by

973 A36-10

Wilcox (2006), which extends (3.7) to all spatial directions. The resulting form is

$$- \bar{\rho}\widetilde{u_j'' T''} = \frac{\mu_t}{Pr_t}\frac{\partial \tilde{T}}{\partial x_j} \rightarrow -\bar{\rho}(u_j'' T'' - \widetilde{u_j'' T''}) = \frac{\mu_t}{Pr_t}\frac{\partial T''}{\partial x_j}. \tag{3.8a}$$

The second approach is a direct application of (3.7), as

$$- \bar{\rho}(u_j'' T'' - \widetilde{u_j'' T''}) = -\frac{1}{Pr_t}\frac{\partial \tilde{T}}{\partial \tilde{u}}\bar{\rho}(u'' u_j'' - \widetilde{u'' u_j''}), \tag{3.8b}$$

which is evaluated using (3.6). Consequently, the heat flux fluctuation is independent of T'' but related to u_i'' instead. Equation (3.8a) is deployed as we prefer to treat T'' as an independent variable. The model using (3.8b) will be discussed in § 7.

Afterward, we focus on the pressure dilatation and dissipation terms in (3.4c). These two also appear in the k'' equation. Little can we learn from the modelling theory on the linearization of pressure dilatation. The budget analysis for k shows that the pressure dilatation and dilatational dissipation in (3.3) are negligible in the supersonic channel cases (Huang *et al.* 1995). So intuitively, their fluctuations are also negligible. The remaining part is the solenoidal dissipation, denoted as $\bar{\rho}\epsilon$. It can be evaluated from, e.g. the k–ϵ model (Jones & Launder 1972), as $\bar{\rho}\epsilon = \bar{\rho}^2 C_\mu k^2/\mu_t$ with C_μ a constant, thus linearized in terms of k''. Note that k'' cannot be expressed as a linear function of $\hat{q}''$, so it needs to be treated as an independent variable, which means that the k'' equation needs to be included in (3.4) to solve the system of six equations. We prefer not to introduce k'' as an independent variable for three reasons. First, there are difficulties in deriving a physically reasonable energy norm for the fluctuation, including k'' (see § 3.3). Second, more terms (e.g. the diffusion term of k'') appear in the k'' equation, and their linearization adds to the uncertainty and complexity of the linear model before a careful assessment. Third, including the k'' equation requires the profile of k as the input, which is harder to obtain than $\tilde{q}$. As an alternative to exclude k'', the turbulent production and dissipation terms can be combined in the spirit of algebraic models (see Appendix A), and the former can be calculated using (3.6). The effects of including k'' will be discussed in § 7.

Finally, there are nonlinear terms N_ρ'', N_{u_i}'' and N_T'' in (3.4), with no counterparts in the modelling theory. These three terms are all related to ρ', so in the spirit of Morkovin's hypothesis, they are of secondary importance. Therefore, they are not linearized but included in the nonlinear forcing. Some supporting evidence will be provided in § 7.

Following the nomenclature for incompressible flows, the linear model utilizing turbulence modelling is termed the eLNS ('e' for eddy-viscosity-enhanced) model. By collecting the residual nonlinearity into the forcing term, the operator form is

$$\frac{\partial \boldsymbol{q}''}{\partial t} = \mathcal{L}_{eLNS}\boldsymbol{q}'' + \boldsymbol{f}_{eLNS}''. \tag{3.9}$$

If using (3.6) and (3.8a) and combining the turbulent production and dissipation terms, then $\mathcal{L}_{eLNS}$ is in the same form as $\mathcal{L}_{LNS}$ except for two substitutions,

$$\tilde{\mu} \rightarrow \tilde{\mu} + \mu_t, \quad \tilde{\kappa} \rightarrow \tilde{\kappa} + \kappa_t = \frac{c_p\tilde{\mu}}{Pr} + \frac{c_p\mu_t}{Pr_t}, \tag{3.10a,b}$$

where κ_t is the eddy diffusivity. Equation (3.10a,b) is used likewise in the algebraic models, and is one of the simplest eLNS models widely used in previous works (Alizard *et al.* 2015; Pickering *et al.* 2021; Chen *et al.* 2023), though the derivation and justification were not elaborated before. Detailed expressions of $\mathcal{L}_{LNS}$ and $\mathcal{L}_{eLNS}$ can be found from

Chen *et al.* (2023). From the mathematical point of view, using (3.10*a,b*) means intensified damping effects due to turbulence, especially in the outer region where $\mu_t \gg \tilde{\mu}$. This point is crucial in understanding the properties of the linear operators in § 4.

Next, we address the calculation of μ_t and Pr_t. From the Boussinesq assumption, μ_t is computed as $\mu_t = -\bar{\rho}\widetilde{u''v''}/(\partial\tilde{u}/\partial y)$. Also, Pr_t is obtained from its definition using $\widetilde{u''v''}$ and $\widetilde{v''T''}$. If the fluctuation statistics are not available, μ_t can be evaluated from the mean streamwise momentum (3.1*b*) as

$$0 = -\frac{d\bar{p}}{dx} + \frac{d}{dy}\left[(\tilde{\mu} + \mu_t)\frac{d\tilde{u}}{dy}\right] \rightarrow \frac{\mu_t}{\tilde{\mu}_w} = \frac{1 - y^+/Re_\tau}{d\tilde{u}^+/dy^+} - \frac{\tilde{\mu}}{\tilde{\mu}_w}. \tag{3.11}$$

For more general flows where (3.11) is inapplicable, μ_t can be estimated using, e.g. the algebraic models. Also, Pr_t can be simply assumed a constant 0.9. In this work, μ_t and Pr_t are determined from the DNS statistics for the benchmark case results. Equation (3.11) and the constant Pr_t are adopted in § 6 for the parameter study.

3.3. *Response to stochastic forcing*

Ensemble-averaged variable correlation $\boldsymbol{\Phi}$ (see (2.7)) is required to compute H_L, γ^2 and A_{pm}^2. Based on § 3.2, $\boldsymbol{\Phi}$ can be obtained by solving a stochastically forced linear system using only mean flow input (Madhusudanan *et al.* 2019). As in (2.3), Fourier decomposition is applied on f'' for the component $\hat{f}''$. After substituting (2.3) into (3.5) or (3.9), the equation for a single mode with $k_x \neq 0$ or $k_z \neq 0$ is

$$\frac{\partial\hat{q}''}{\partial t} = \hat{\mathcal{L}}\hat{q}'' + \hat{f}'', \tag{3.12}$$

where $\hat{\mathcal{L}}(\tilde{q}, k_x, k_z)$ can be either $\hat{\mathcal{L}}_{LNS}$ or $\hat{\mathcal{L}}_{eLNS}$, $\hat{f}'' = [\hat{f}''_\rho, \hat{f}''_u, \hat{f}''_v, \hat{f}''_w, \hat{f}''_T]^T$ is the forcing term and $\hat{q}''$ is the response. The energy norm of $\hat{q}''$ is defined as (Chu 1965)

$$\|\hat{q}''\|^2 = (\hat{q}'', \hat{q}'')_E = \int_0^{2h}\left(\bar{\rho}\hat{u}''^H\hat{u}'' + \frac{R\tilde{T}}{\bar{\rho}}\hat{\rho}'^\dagger\hat{\rho}' + \frac{\bar{\rho}c_v}{\tilde{T}}\hat{T}''^\dagger\hat{T}''\right)dy = \int_0^{2h}\hat{q}''^H\boldsymbol{M}\hat{q}''\,dy, \tag{3.13}$$

where $\boldsymbol{M}$ is the energy weight matrix.

When (3.12) is driven by a stochastic forcing, the response is also stochastic if the system is linearly stable. Following those for incompressible flows (Gupta *et al.* 2021), the forcing is $\hat{f} = \boldsymbol{B}\hat{f}_0$ where $\boldsymbol{B}(y)$ is a modelling matrix and $\hat{f}_0$ is a white noise signal. Specifically, $\hat{f}_0$ is assumed to be a δ-correlated Gaussian white noise with zero mean,

$$\langle\hat{f}''_0\rangle = 0, \quad \langle\hat{f}''_0(y, t)\hat{f}''^H_0(y', t')\rangle = \boldsymbol{I}\delta_d(y - y')\delta_d(t - t'), \tag{3.14}$$

where $\boldsymbol{I}$ is the identity matrix and δ_d is the Dirac function. The introduction of $\boldsymbol{B}(y)$ allows for varying forcing amplitude for different variables at different y. The specific expression of $\boldsymbol{B}$ will be provided later in (3.17). Mathematically, $\boldsymbol{\Phi}$ is obtained by solving the algebraic Lyapunov equation (see Farrell & Ioannou (1993) for more details) as

$$\hat{\mathcal{L}}\boldsymbol{\Phi} + \boldsymbol{\Phi}\hat{\mathcal{L}}^\dagger + BB^H = \boldsymbol{0}. \tag{3.15}$$

Note that $\hat{\mathcal{L}}$ contains wall-normal derivatives, so $\hat{\mathcal{L}}^\dagger$ is defined in an adjoint manner. Also, the vector product is with respect to (3.13). Equation (3.15) is discretized using the Chebyshev collocation point method. By default, $N_y = 301$ points are used, abundant to

ensure grid independence (Bae *et al.* 2020). The Lyapunov equation is solved using the MATLAB software. For boundary conditions, a no-slip, isothermal wall is assumed on both sides. Therefore, the wall fluctuations satisfy $\hat{u}''_w = \hat{v}''_w = \hat{w}''_w = \hat{T}''_w = 0$, and $\hat{\rho}'_w$ is solved through the continuity equation. The solver verification can be found from Chen *et al.* (2023).

In the incompressible model of Madhusudanan *et al.* (2019), $\boldsymbol{B}$ is set to $\boldsymbol{I}$ for both LNS and eLNS, meaning that the stochastic forcing has uniform amplitude along the wall-normal direction. This is also adopted in previous compressible works (Alizard *et al.* 2022; Chen *et al.* 2023). To improve the estimation below the logarithmic region, Gupta *et al.* (2021) design two new models for incompressible flows, termed 'W-model' and 'λ-model', where $\boldsymbol{B}$ is y-dependent or even scale-dependent. The simpler W-model is considered here, where the forcing amplitude for the momentum equation varies in proportion to $\nu_t = \mu_t/\bar{\rho}$. For compressible flows, $\tilde{f}_\rho$ and $\tilde{f}_T$ are present and need to be modelled. Without comprehensive knowledge of the forcing statistics, we consider the simplest form here, which is instructive and free from *ad hoc* implementations. First, $\boldsymbol{B}$ is set to be diagonal, i.e. $\boldsymbol{B} = diag([B_\rho \; \nu_t \; \nu_t \; \nu_t \; B_T]^{\mathrm{T}})$, where the amplitude functions B_ρ and B_T are to be determined. In this way, the off-diagonal terms, i.e. the cospectra of the forcing components and also the anisotropy (Foysi, Sarkar & Friedrich 2004), are not modelled. Second, $\boldsymbol{B}$ is assumed to be only related to the mean flow, independent of length scales λ_x and λ_z. The extended SRA (3.7) and the DNS data of Coleman *et al.* (1995) suggest that the following relations are nearly satisfied:

$$T''_{rms} = \frac{1}{Pr_t} \left| \frac{\partial \tilde{T}}{\partial \tilde{u}} \right| u''_{rms}, \quad \rho'_{rms} = \frac{1}{Pr_t} \left| \frac{\partial \bar{\rho}}{\partial \tilde{u}} \right| u''_{rms} \approx \frac{\bar{\rho}}{Pr_t \tilde{T}} \left| \frac{\partial \tilde{T}}{\partial \tilde{u}} \right| u''_{rms}, \qquad (3.16a,b)$$

where the subscript *rms* is for root mean square, and the approximation is due to the slightly varying mean pressure. The mean flow gradients appear in their absolute values because the fluctuation r.m.s. is positive. For channel flows, $\partial \tilde{T}/\partial \tilde{u} > 0$ and $\partial \bar{\rho}/\partial \tilde{u} < 0$ hold in the whole field. From (3.16a,b), the forcing amplitude is modelled as

$$\boldsymbol{B} = diag\left(\left[\frac{1}{Pr_t} \frac{\partial \bar{\rho}}{\partial \tilde{u}} \nu_t, \; \nu_t, \; \nu_t, \; \nu_t, \; \frac{1}{Pr_t} \frac{\partial \tilde{T}}{\partial \tilde{u}} \nu_t \right]^{\mathrm{T}} \right). \qquad (3.17)$$

Since the SLSE quantities in § 2.3 contain only the ratios of cospectra, multiplying $\boldsymbol{B}$ by a non-zero constant does not affect the SLSE results. The examination for (3.16a,b) is shown in figure 2 using the present DNS data (benchmark case). Both ρ'_{rms} and T''_{rms} from (3.16a,b) are in line with DNS, though ρ'_{rms} is slightly underestimated. Notably, the fact that ρ'_{rms} and T''_{rms} are primarily determined by u''_{rms} and their mean flow gradients hints that they are advection dominated. The larger deviation in the outer region indicates more pronounced thermodynamic processes where the mean flow gradients are small and the local Mach number is high.

In summary, two linear models used in this work are (1) the LNS model (3.5) and (2) the eLNS model ((3.9) and (3.10a,b)). In both cases, (3.17) is used for variable control. There is also a notation 'eLNS-CD' below, to be introduced in § 5.4. In § 3.1, we use the Favre averages to derive the linear model, so we should also use $\tilde{q}$ to calculate $\hat{\mathcal{L}}$ and then $\boldsymbol{\Phi}$. As Ma_b here is relatively low, the difference between $\tilde{q}$ and $\bar{q}$ is very small (Huang *et al.* 1995; Cheng & Fu 2022b). We have compared $\boldsymbol{\Phi}$ using the two mean flows, and the relative difference is less than 1 %. Thereby, for ease of later comparison with the ODE-based mean flow (§ 6), we will use $\bar{q}$ to compute $\tilde{\mathcal{L}}$ and $\boldsymbol{\Phi}$ throughout.
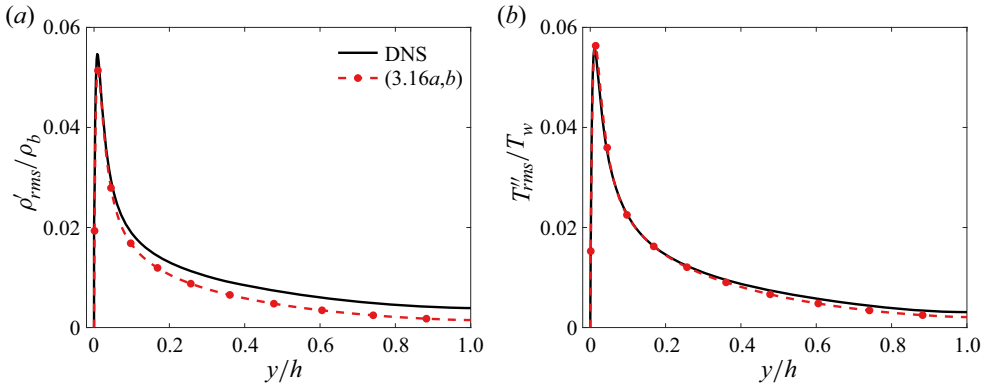
Figure 2. Wall-normal distributions of the (*a*) density and (*b*) temperature fluctuations (r.m.s.) from the DNS data and (3.16*a,b*). Note that u''_{rms} is also from DNS.

4. Properties of the linear operator

As introduced in § 3.2, the linear operators $\hat{\mathcal{L}}_{LNS}$ and $\hat{\mathcal{L}}_{eLNS}$ were considered in previous works, but their mathematical features were not elaborated. The framework in § 3.3 requires a globally stable system, and the response amplification depends on the non-normality of the linear operator (Trefethen 1997). Thereby, we scrutinize the eigenspectra and pseudospectra of the linear operators in this section. The categorization of different modes is also discussed. Significant differences will be noted from the incompressible case, and the discussions have important implications for later SLSE results.

4.1. *Spectra of the linear operator*

From (3.12), the eigenvalues of $\hat{\mathcal{L}}$ reflect the temporal modal instability of $\hat{q}''$, defined as $\hat{\mathcal{L}}\breve{q}'' = -i\omega\breve{q}''$. Here $\omega = \omega_r + i\omega_i$ is the eigenvalue with ω_r the frequency and ω_i the growth rate, and $\breve{q}''$ is the right-eigenfunction. The eigenspectra of $\hat{\mathcal{L}}_{LNS}$ and $\hat{\mathcal{L}}_{eLNS}$ are displayed in figures 3(*a*) and 3(*b*) at $\lambda_x = 8h$ and $\lambda_z = 2h$. As will be shown in § 5, the LCS at this (λ_x, λ_z) is approximately the highest within the length scales considered. All the eigenmodes in figure 3 are stable ($\omega_i < 0$), meeting the requirement of a globally stable system. The distributions of ω_r are similar between the LNS and eLNS spectra. A prominent difference is that the damping rates $|\omega_i|$ of the eLNS modes are nearly two orders of magnitude higher. This is because after the substitutions in (3.10*a,b*), the damping second-order derivative terms are highly increased. The proof from the growth-rate decomposition is provided in Appendix C to support the explanation.

Next, the categorization of eigenmodes is discussed, which is crucial for interpreting later linear-model results. The classic four mode branches are identified in both LNS and eLNS spectra, namely the vortical, entropy, and fast and slow acoustic branches, as denoted in different colours (Balakumar & Malik 1992). Notably, the term vortical branch hereinafter is not restricted to vortices but a general term for all kinematically dominated modes, analogous to the incompressible case. The reference frequencies of four branches, as labelled in figure 3, are obtained by solving the fluctuations on an inviscid uniform
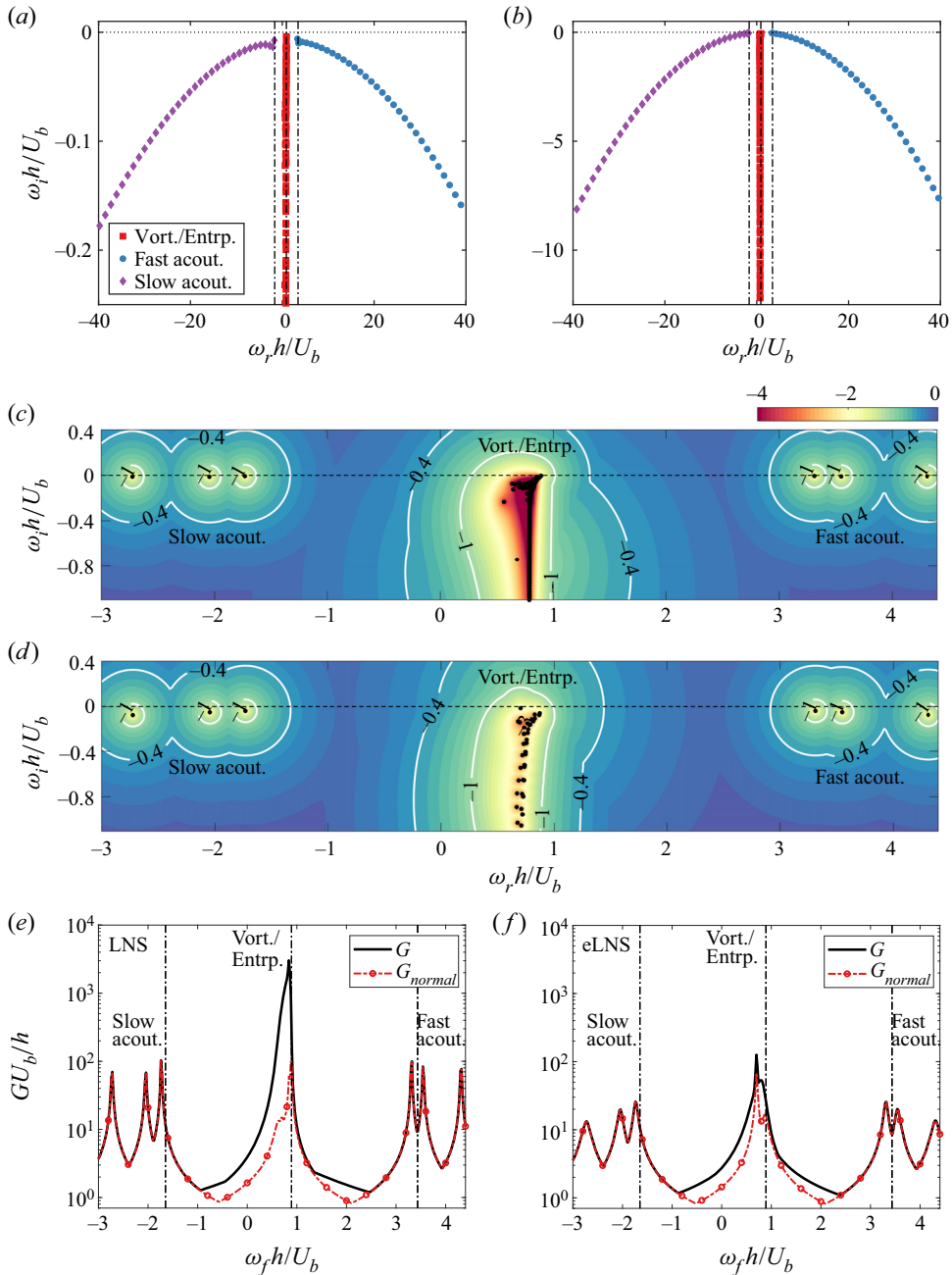
973 A36-14

Figure 3. (*a,b*) Spectra, (*c,d*) pseudospectra ($\log_{10}\varepsilon$), and (*e,f*) the maximum response gain of the linear operators for (*a,c,e*) LNS and (*b,d,f*) eLNS in the benchmark case ($\lambda_x = 8h$, $\lambda_z = 2h$). The vertical dashed lines in (*a,b,e,f*) are from (4.1), and the black dots in (*c,d*) denote the eigenvalues.

mean flow, as

$$\left.\begin{array}{ll} \omega_{r,vort} = \omega_{r,ent} = \tilde{u}_c k_x & \text{for vortical, entropy modes,} \\[2mm] \omega_{r,acout} = \tilde{u}_c\left(k_x \pm \dfrac{1}{Ma_c}\sqrt{k_x^2 + k_z^2}\right) & \text{for fast/slow acoustic modes,} \end{array}\right\} \quad (4.1)$$
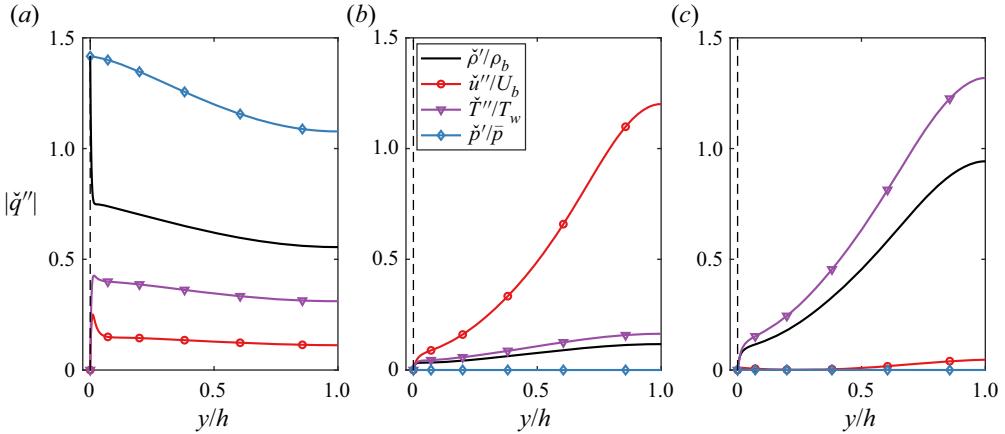
Figure 4. Eigenfunctions of the linear operator in the eLNS model ($\lambda_x = 8h$, $\lambda_z = 2h$): (*a*) acoustic mode ($\omega h/U_b = 3.312 - 0.038i$); (*b*) vortical mode ($\omega h/U_b = 0.870 - 0.059i$) and (*c*) entropy mode ($\omega h/U_b = 0.866 - 0.075i$).

where the subscript c denotes the channel centre ($y = h$), analogous to the free stream in boundary layers. The derivation for (4.1) and corresponding eigenfunctions are detailed in Appendix B. In the free stream, the acoustic modes are isentropic and dilatational, the entropy modes are isobaric and static, and the vortical modes are solenoidal with zero thermodynamic components, so they can be easily distinguished. In the channel flow, however, these modes are more complicated due to the non-uniform mean flow and viscosity. For illustration, figure 4 plots the eigenfunctions of the least stable vortical, acoustic and entropy modes in the eLNS spectra, where the linearized pressure fluctuation $\check{p}'/\bar{p} = \check{\rho}'/\bar{\rho} + \check{T}''/\tilde{T}$. The modes of lower ω_i exhibit common features. The acoustic modes (figure 4*a*) can be recognized from others based on ω_r. Also, they have large pressure fluctuations, while the vortical and entropy modes are nearly isobaric. There are a series of acoustic modes in figure 3 with different wall-normal wavenumbers (k_y), and $\omega_{r,acout}$ in (4.1) represents the lower (upper) frequency limit with zero k_y for the fast (slow) branches. In comparison, the vortical and entropy modes have close ω_r, so they cannot be distinguished directly in figure 3. The vortical modes (figure 4*b*) have large velocity components, and the non-zero $\check{\rho}'$ and $\check{T}''$ are mainly from the passive advection due to mean-flow gradients. Their entropy fluctuations are also non-zero since the mean flow is not isentropic. In contrast, the entropy modes (figure 4*c*) are dominated by the thermodynamic components, while their velocity components are not zero due to the viscous and diffusive terms. The vortical modes are not isentropic and the entropy modes are kinematic, so they can be coupled with each other and the modes with smaller ω_i in the vortical/entropy branch may not be as clearly distinguished as in figure 4. The eigenfunctions of different types of modes in the LNS model are similar in shapes to figure 4. The differences are contributed by the eddy terms related to μ_t and κ_t (see Appendix B). The effects of different modes on the response behaviour will be further discussed in § 4.2.

4.2. *Pseudospectra of the linear operator*

All the eigenmodes of $\hat{\mathcal{L}}$ are asymptotically stable, so its transient behaviour is determined by external forcing and the non-normality of the linear operator (Trefethen 1997).

The ε-pseudospectra is a quantitative measure of non-normality. By definition, a smaller ε means that the eigenvalues are more sensitive to perturbations on $\hat{\mathcal{L}}$, so the non-normality is stronger. Also, in response to a harmonic external forcing of frequency ω_f, ε measures the largest gain of the response $G(\omega_f) = max\|(-\mathrm{i}\omega_f \boldsymbol{I} - \hat{\mathcal{L}})^{-1}\|$, which equals $1/\varepsilon_0$ with ε_0 the ε at the imaginary axis (see Chomaz (2005), for more details). The pseudospectra and $G(\omega_f)$ of the two linear operators are depicted in figures 3(c)–3(f) to provide insights into the response characteristics. To distinguish from the resonant effects, the gain if $\hat{\mathcal{L}}$ is normal, $G_{normal}(\omega_f)$, is also plotted. For the LNS case, strong non-normality appears for the vortical modes since G can be over one order of magnitude higher than G_{normal}, which is known to be an essential feature of the Orr–Sommerfeld operator. The non-normality of the entropy modes cannot be directly measured because their ω are close to the vortical modes. In comparison, the acoustic modes are of little non-normality as G results mostly from the resonant effects. Therefore, we can expect that the behaviour of $\hat{q}''$ is largely determined by the vortical modes, similar to the incompressible case. Hanifi, Schmid & Henningson (1996) show that including the acoustic modes or not negligibly affects the transient growth results for a laminar flow (LNS case). A similar examination will be performed later for the turbulent mean flow in the stochastically driven system. When the linear operator is eddy viscosity enhanced (figures 3d and 3f), the non-normality of the acoustic modes is slightly affected, but that of the vortical (and possibly entropy) modes is severely weakened, reflected from the larger ε and much smaller G/G_{normal}. Consequently, the acoustic (and also entropy) modes, and thus the compressibility effects, are expected to play more vital roles in the fluctuation evolution.

It is worth mentioning that Symon *et al.* (2021) and Kuhn *et al.* (2022) also report in their incompressible cases that eddy viscosity decreases the non-normality of the linear operator for structures of high λ_x/λ_z. Symon *et al.* (2021) conclude that this effect of counteracting non-normality in the eLNS model mitigates the trade-off between turbulent production and nonlinear energy transfer, leading to better prediction for streamwise-elongated structures than the LNS model. In the compressible case studied here, however, additional acoustic and entropy modes are present, so the weakened non-normality of the vortical modes can lead to more complicated consequences.

To support the above observations and further quantify the effects of acoustic and entropy modes, the energy amplification factor of the response V is computed. Here, V is defined as the variance of $\hat{q}''$, obtained as the trace of $\boldsymbol{\Phi}$ with respect to the energy norm (Hwang & Cossu 2010). Two V are needed, with acoustic (or entropy) modes included and excluded, respectively, to distinguish their contributions. Equation (3.15) contains the contributions of all modes, so a framework needs to be developed first that can give the cospectra considering only partial modes. Following that in the transient growth analysis (Hanifi *et al.* 1996), the response is restricted to the space spanned by partial eigenfunctions,

$$\hat{q}'' \approx \sum_{m=1}^{N_m} c_m(t)\breve{q}''_m = \breve{Q}'' C(t), \tag{4.2}$$

where m and N_m are the indexes and total number of the modes selected, and c_m is a time-dependent coefficient. In matrix form, $\breve{Q}'' = [\breve{q}''_1, \ldots, \breve{q}''_{N_m}]$ and $C = [c_1, \ldots, c_{N_m}]^{\mathrm{T}}$. The resulting cospectrum is $\boldsymbol{\Phi} = \langle \hat{q}'' \hat{q}''^H \rangle = \breve{Q}'' \langle CC^H \rangle \breve{Q}''^H$. Similar to (3.15), the governing equation for $\langle CC^H \rangle$ is derived as

$$\boldsymbol{\Lambda} \langle CC^H \rangle + \langle CC^H \rangle \boldsymbol{\Lambda}^H + [\breve{Q}''^H (BB^H)^{-1} \breve{Q}'']^{-1} = \boldsymbol{0}, \tag{4.3}$$
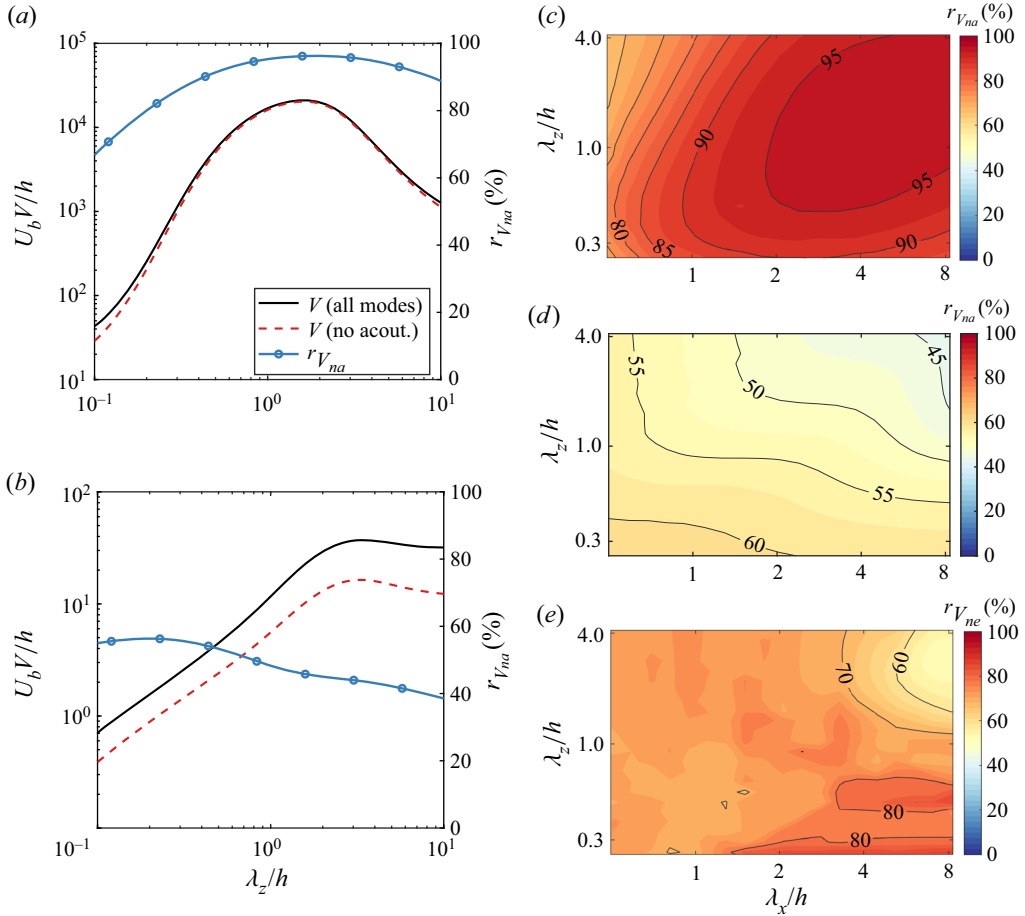
973 A36-17

Figure 5. (*a*,*b*) Energy amplification factors for all modes (V) and when acoustic modes are excluded (V_{nacout}) (left axis) and their ratio $r_{V_{na}} = V_{nacout}/V$ (right axis) at different spanwise wavelengths ($\lambda_x = 8h$), and the contours of (*c*,*d*) $r_{V_{na}}$ and (*e*) $r_{V_{ne}} = V_{nentrp}/V$ at different length scales. Panels (*a*,*c*) are for the LNS model and (*b*,*d*,*e*) are for eLNS.

where $\boldsymbol{\Lambda} = diag([\omega_1, \ldots, \omega_{N_m}])$. Therefore, the response when only partial eigenmodes are included can be obtained by solving (4.3). Note that $\boldsymbol{BB}^H$ can be non-invertible as the element ν_t in (3.17) tends to zero at the wall. A small positive constant is added to the diagonal of $\boldsymbol{B}$ for solving (4.3) only to avoid the singularity. Also, one drawback of (4.3) is its inapplicability to the highly non-normal case where $\check{Q}''^H \check{Q}''$ has a very large condition number, hence nearly non-invertible.

Figures 5(*a*) and 5(*b*) plot the distributions of V for the LNS and eLNS models at different λ_z ($\lambda_x = 8h$). The V in the LNS case is over one order of magnitude higher than that in the eLNS case, consistent with the stronger non-normality in figure 3(*c*). Note that the higher V in the LNS case does not directly influence the SLSE quantities since they contain only the ratios of cospectra. The effects of acoustic modes are studied first. In figure 5(*a*), the energy growth with acoustic modes excluded (V_{nacout}) is quite close to V, supporting the observation in figures 3(*c*) and 3(*e*) that the acoustic modes are in secondary roles for the linear operator in terms of non-normality. As a quantitative measure, the ratio $r_{V_{na}} = V_{nacout}/V$ is plotted in percentage. In most of the λ_z range

973 A36-18

displayed, the non-acoustic components contribute over 90 % of the total energy growth of the response, similar to the laminar case (Hanifi *et al.* 1996). For the eLNS model in figure 5(*b*), however, the non-acoustic components contribute only approximately 50 % of the total energy growth, and the contributions of acoustic modes are prominent, consistent with the inference from figures 3(*d*) and 3(*f*).

To gain further knowledge on the scale dependence of the acoustic-mode effects, the contours of $r_{V_{na}}$ are depicted in figures 5(*c*) and 5(*d*) for the two models. The λ_x and λ_z ranges displayed are of interest for SLSE, as will be specified in § 5. The $r_{V_{na}}$ in the LNS case is over 80 % in most scale ranges, while that in the eLNS case is within 45 % to 60 %. More importantly, $r_{V_{na}}$ tends to increase at a larger scale in the LNS model, and is over 95 % when $\lambda_x > 2h$ and $\lambda_z > 0.5h$. In contrast, $r_{V_{na}}$ diminishes as λ_x and λ_z rise in the eLNS model, indicating that the large-scale structures are especially affected by the acoustic modes. In the same way, the effects of entropy modes are quantified in figure 5(*e*) for the eLNS case, using $r_{V_{ne}} = V_{nentrp}/V$ with V_{nentrp} the energy growth excluding entropy modes. The $r_{V_{ne}}$ in the LNS case is not displayed as the matrix excluding the entropy modes is highly non-normal (see figure 3*c*). In the eLNS case, $r_{V_{ne}}$ is within 60 % to 80 % in most scale ranges, so the entropy modes are also non-negligible for the response growth, though their influences are weaker than the acoustic modes since $r_{V_{ne}} > r_{V_{na}}$. Note that the contours of $r_{V_{ne}}$ are not as smooth as $r_{V_{na}}$ in figure 5(*d*), due to the coupling effects between the vortical and entropy modes, as discussed in § 4.1. Nevertheless, the qualitative trend in figure 5(*e*) is not affected. The entropy-mode effect in the LNS case is not demonstrated, so its difference from the eLNS case is not reflected. The results in § 5 suggest that the acoustic components play a larger role than the entropy ones for SLSE in the present case, so the difference of $r_{V_{na}}$ (figures 5(*c*) and 5(*d*)) is important, and the acoustic components will be more focused on below.

We provide more interpretations on the trends in figure 5. For an inviscid uniform mean flow (free stream, $\tilde{\mu} = \mu_t = 0$), the eigenfunctions of different modes in (4.1) are perpendicular to each other under the energy norm in (3.13), so $\hat{\mathcal{L}}$ is normal (George & Sujith 2011). It becomes non-normal in the presence of mean flow gradients and viscosity. The latter two effects are the strongest in the near-wall region, while the acoustic and entropy modes are prevailing in the outer region, so the non-normality between the vortical and other three branches is weak (figure 3*c*). Meanwhile, as λ_x and λ_z increase from small scales, the amplified structure moves away from the wall into the outer region. The decrease of mean flow gradients leads to less coupled mode branches and thus increasing $r_{V_{na}}$ (closer to the free stream condition), as observed in figure 5(*c*). When the model is μ_t-enhanced (eLNS), however, the trends are reversed simply because μ_t is zero at the wall and largest in the outer region with $\mu_t \gg \tilde{\mu}$ ($\sim$70 times in the present case). This means, from the view of equations, that the damping effects due to the modelled eddy terms are highly intensified ($\tilde{\mu} \rightarrow \tilde{\mu} + \mu_t$). Consequently, the larger-scale structure is more affected by μ_t, and the dissipative second-order derivative terms for μ_t result in strong coupling between the acoustic, entropy modes and others. This is exactly what we observe in figures 5(*d*) and 5(*e*).

In summary, there are four branches of eigenmodes in both LNS and eLNS cases, and the vortical branch has strong non-normality to support the transient behaviour of the fluctuations (response) subject to stochastic forcing. For the LNS model, the acoustic modes have little non-normality and increasingly small contributions to the energy growth as the length scales (both λ_x and λ_z) increase. In contrast, the non-normality of the vortical modes diminishes in the eLNS model due to the damping effects of μ_t on the eigenmodes. As a result, the acoustic and entropy modes can account for 20 % to 55 % of the energy

growth; their contribution goes higher for larger-scale structures. The above is a significant difference between the LNS and eLNS models, not present in incompressible flows.

For the eLNS model, the fact that the acoustic and entropy modes, and thus compressibility effects, can have such a high contribution to the fluctuation growth deserves serious concern, considering the great similarities reported before to incompressible flows (see § 1). We examine below whether this prominent role of acoustic and entropy components in the eLNS model is an intrinsic defect introduced by turbulence modelling, through comparison with DNS. In fact, we show in § 5 that the prominent acoustic and entropy components can be problematic, especially for the density/temperature fields, and will seek remedies.

5. General flow structures and SLSE results

5.1. *General flow structures*

We first present an overview of the general structures of velocity and temperature fields in the benchmark case. Comprehensive analyses have been reported in previous works based on experiments and DNS for both channel and boundary-layer flows (Smith & Smits 1995; Ringuette *et al.* 2008; Pirozzoli & Bernardini 2011; Cogo *et al.* 2022; Cheng & Fu 2023*a*), so here we only provide a brief description to set the grounds for later discussions.

After the velocity transformation of Griffin *et al.* (2021), the mean streamwise velocity $\tilde{u}_{GFM}^+(y^*)$ matches the universal incompressible profile $\bar{u}_{incp}^+(y^+)$ within and below the logarithmic region, as shown in figure 6(*d*). Therefore, we can follow the criterion in incompressible flows to name different regions in terms of y^* and y/h. Three wall-normal heights are selected, namely $y^* = 11$ in the buffer layer (near-wall region), $y^* = 107$ ($y = 0.14h$) in the logarithmic layer and $y = 0.5h$ ($y^* = 385$) in the outer region, to display the instantaneous fields in different regions using DNS. Hence, the overall flow organization can be recognized. Notably, Abe & Antonia (2017) show in their incompressible case that $y \approx 0.5h$ is the region where large-scale structures of the streamwise velocity and temperature (as a passive scalar) fluctuations dominate. In the near-wall region (figures 6*c* and 6*g*), both u''^+ and T''^+ exhibit streamwise-elongated streaks, connected with the 'sweep' and 'ejection' events in the near-wall self-sustaining cycles (Hamilton, Kim & Waleffe 1995; Schoppa & Hussain 2002). Meanwhile, u''^+ and T''^+ strongly resemble each other morphologically. As a quantitative measure, Cheng & Fu (2023*a*) show that the correlation coefficient of u''^+ and T''^+, $R_{u''T''} = \langle u''T'' \rangle / (u''_{rms}T''_{rms})$, is approximately one at $y^* \lesssim 12$. Further away from the wall into the logarithmic region (figures 6*b* and 6*f*), dominant velocity streaks are in larger length scales, while the streamwise-elongated feature is less obvious for T''. In other words, T'' is more isotropic than its near-wall counterpart, filled with jellyfish-shaped structures. The observation position in figures 6(*a*) and 6(*e*) is out of the logarithmic region. Large scale u'' streaks are still identifiable, but streamwise T'' streaks are hardly seen with obvious spanwise extensions. Cheng & Fu (2023*a*) demonstrate that the spanwise length scales of u'' and T'' corresponding to their pre-multiplied spectra peaks are actually comparable to each other throughout the channel; T'' has a shorter peak streamwise length scale within and above the logarithmic region, thus tending to be more isotropic.

In the following, we focus on predicting the coherent velocity and temperature fluctuations using SLSE based on the measurement at outer locations. Here y_m^* is fixed at the centre of the logarithmic region (Marusic *et al.* 2010), and the estimations are conducted at $y_p^* < y_m^*$. In analogy to the incompressible flow (Townsend 1976), the centre of the logarithmic region is evaluated to be $3.9Re_\tau^{*1/2}$, which gives $y_m^* = 107$.
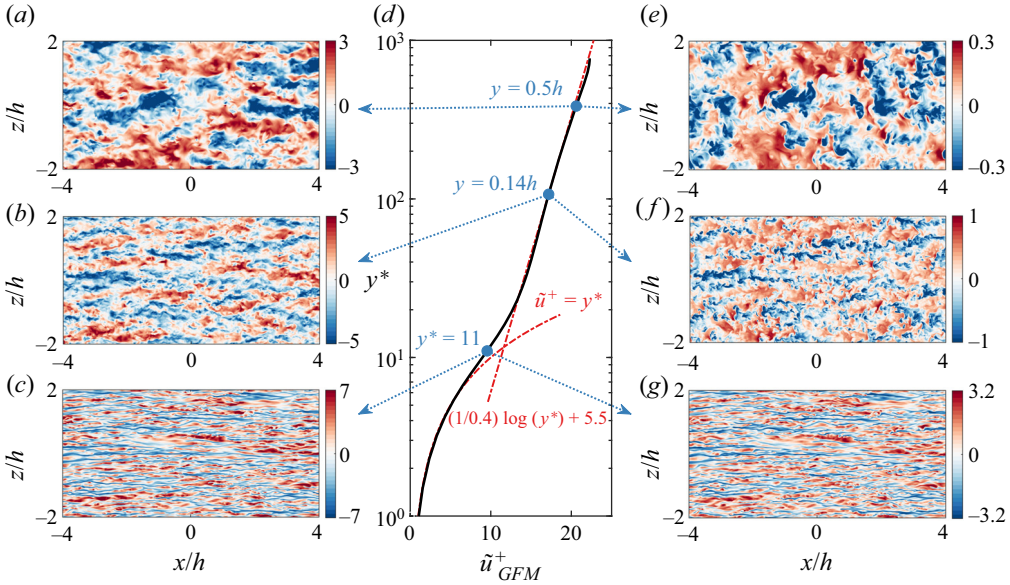
Figure 6. Overview of the turbulent field for the benchmark case: $(a–c)$ instantaneous streamwise velocity fluctuation (u''^+), (d) transformed mean velocity profile and $(e–g)$ instantaneous temperature fluctuation (T''^+); (a,e) are at $y = 0.5h$ $(y^* = 385)$, (b,f) are at $y = 0.14h$ $(y^* = 107)$ and (c,g) are at $y^* = 11$ (top view).

5.2. *Estimation for streamwise velocity*

The two components of $H_{L,uu}$, i.e. γ_{uu}^2 and $A_{pm,uu}$, are calculated first. They describe the spectral coherence and amplitude ratio of $\hat{u}''$ at different heights. Afterwards, $H_{L,uu}$ is used to estimate the instantaneous field. In general, the SLSE results for $\hat{u}''$ from DNS and linear models closely resemble those from the incompressible case (Madhusudanan *et al.* 2019; Gupta *et al.* 2021), so the discussion is presented briefly, highlighting crucial points.

Panels $(a–c)$ in figures 7 and 8 are the results from the DNS data. The three estimation locations are $y_p^* = 70$, 40 and 10, ranging from the logarithmic layer down to the buffer layer. Limited by the computational domain, the largest length scales displayed are $\lambda_x \approx 8h$ and $\lambda_z \approx 4h$. As in incompressible flows (Baars *et al.* 2016; Madhusudanan *et al.* 2019), large-scale structures have stronger coherence than the small scale, especially in the streamwise direction. This is in line with figure 6 where the streamwise-elongated streaky motions dominate the instantaneous velocity field. Meanwhile, the coherence is weakened with the decrease of y_p^* (figures 7a–7c), simply because y_m^* and y_p^* are farther apart. At $y^* = 10$, the region with $\gamma_{uu}^2 > 0.5$ only appears at $\lambda_x > 4h$, or $\lambda_x^* > 3600$, which is much larger than the dominant length scale of the u'' streaks ($\lambda_x^* \approx 1000$, Yao & Hussain 2020). However, though close to the wall, the motion of the largest scale is still coherent with that at $y_m^* = 107$, reminiscent of the AEM. From figures 8(b) and 8(c), the structures with $\lambda_z < 0.5h$ have relatively large $A_{pm,uu}$, which means narrow (in terms of λ_z) streaky motions are continuously enhanced approaching the wall. This is consistent with figure 6 where the fluctuation amplitude rises as y^* decreases.

We next focus on the linear model results. In general, γ_{uu}^2 and $A_{pm,uu}$ from the eLNS model are closer to DNS than the LNS model. By considering the wall-normal variation of the forcing amplitude (3.17), γ_{uu}^2 and $A_{pm,uu}$ near the wall can also be well predicted by eLNS, as shown in figures 7(i) and 8(i), though $A_{pm,uu}$ at small λ_z ($\lesssim 0.5h$) tends to be under-predicted. In comparison, the LNS results have increasingly larger deviations
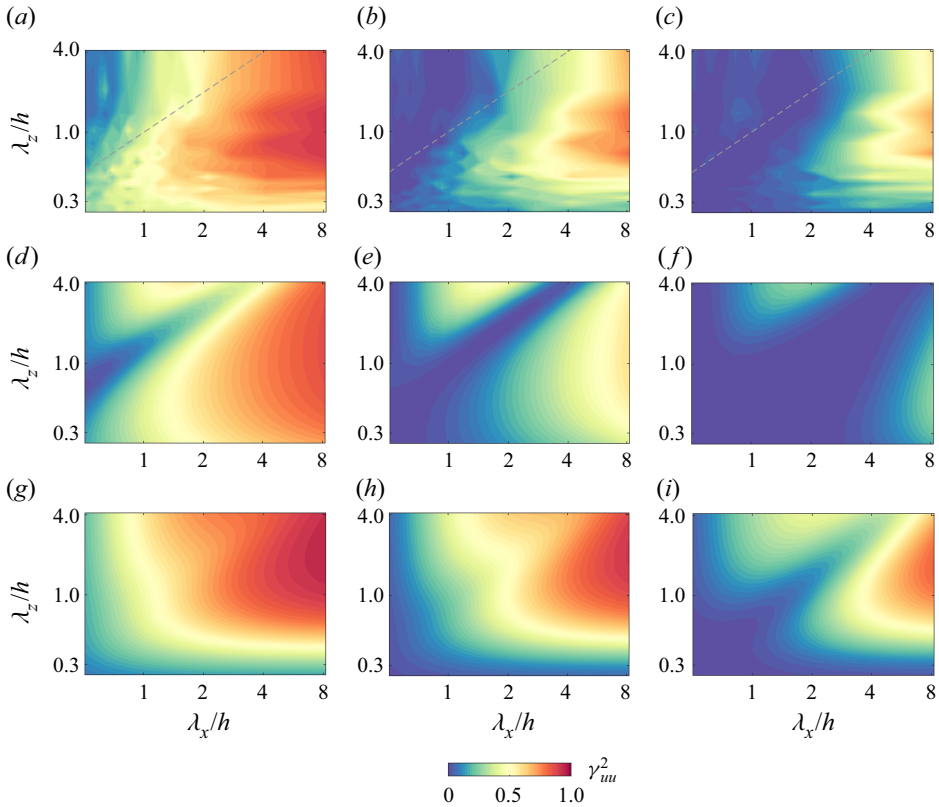
Figure 7. Contours of 2-D LCS for u'' ($y_m^* = 107$) at (a,d,g) $y_p^* = 70$, (b,e,h) $y_p^* = 40$ and (c,f,i) $y_p^* = 10$. Panels $(a-c)$ are from the DNS data, $(d-f)$ are from the LNS model and $(g-i)$ are from the eLNS model. The dotted lines denote $\lambda_x = \lambda_z$.

towards the wall, and γ_{uu}^2 and $A_{pm,uu}$ are both underestimated. In particular, $A_{pm,uu}$ is smaller than unity, i.e. $\langle |\hat{u}_p''|^2 \rangle < \langle |\hat{u}_m''|^2 \rangle$ in most regions in figures 8(e) and 8(f), which is opposite to the DNS trend. This indicates that the structures modelled by LNS are localized in the wall-normal direction. The introduction of μ_t enhances the structural coherence between different heights, and can reasonably reflect the wall-normal coherence and amplitude variation of the velocity fluctuations. Notably, in the region $\lambda_x < \lambda_z$, γ_{uu}^2 in the eLNS model has some deviations from the DNS data, not present in incompressible cases. This difference is related to compressibility effects and will be further discussed in § 6.

After obtaining H_L, the large-scale coherent portion of the instantaneous field u_p'' at y_p^* can be estimated using (2.4a) and the DNS snapshots u'' at y_m^*, reflecting the superposition effects in IOIM. As pointed out by Baars *et al.* (2016), the scales at very small γ^2 can be erroneously estimated due to the possibly large H_L, then one may obtain intense small-scale motions in some regions of little coherence with the fields measured. To avoid this, a threshold $\gamma_{th}^2 = 0.05$ is introduced, and H_L with $\gamma^2 < \gamma_{th}^2$ is forced to zero (Madhusudanan *et al.* 2019). In this way, the small-scale motions of little coherence are artificially ruled out. The resulting snapshots of $u_p''^+$ at $y_p^* = 70$ and 10, estimated from
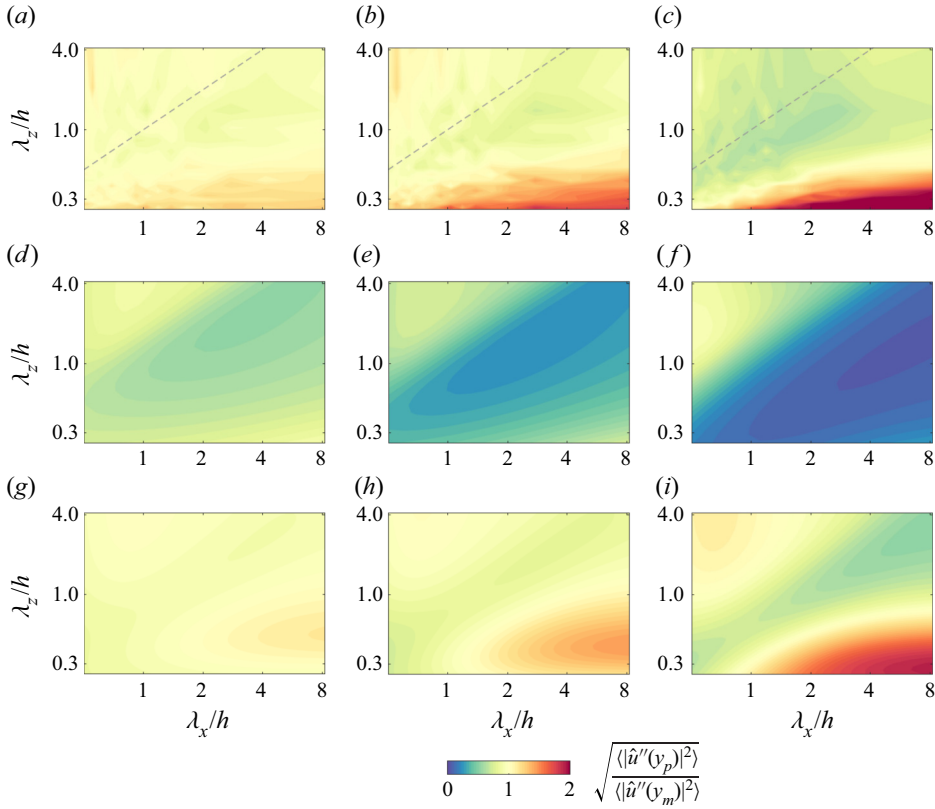
973 A36-22

Figure 8. Contours of the amplitude ratio for u'' ($A_{pm,uu}$, $y_m^* = 107$) at (a,d,g) $y_p^* = 70$, (b,e,h) $y_p^* = 40$ and (c,f,i) $y_p^* = 10$. Panels (a–c) are from the DNS data, (d–f) are from the LNS model and (g–i) are from the eLNS model. The dotted lines denote $\lambda_x = \lambda_z$.

different models, are depicted in figure 9. The corresponding 2-D velocity spectra of $u_p''^+$,

$$\Phi_{u_p u_p}^+(y_p) = \langle \hat{u}_p''^+(y_p) \hat{u}_p''^{+\dagger}(y_p) \rangle = |H_{L,uu}(y_p, y_m)|^2 \langle \hat{u}''^+(y_m) \hat{u}''^{+\dagger}(y_m) \rangle_{DNS}, \quad (5.1)$$

are also shown for more quantitative evaluation. Compared with figures 6(b) and 6(c), small-scale structures ($\lambda_x \lesssim h$, $\lambda_z \lesssim 0.3h$) are nearly missing in figures 9(a) and 9(d) due to the weak coherence at those scales, hence not considered by the superposition effects. Also, the dominant structures in figures 9(a) and 9(d) have similar λ_x and λ_z. These footprints posed by the motions at y_m^* on y_p^* are crucial in the IOIM (Baars *et al.* 2016). For the linear models, the eLNS results in figures 9(c) and 9(f) bear a strong resemblance to the DNS counterparts, which is expected from the relative agreement of γ_{uu}^2 and $A_{pm,uu}$ in figures 7 and 8. Nevertheless, the structures of $\lambda_z \lesssim 0.5h$ are somewhat underestimated, which may be improved by further modelling the scale dependence of $\boldsymbol{B}$ (Gupta *et al.* 2021). In comparison, the LNS model estimates weak u''^+, especially down to the buffer layer. The velocity field and 2-D spectrum in figure 9(e) are nearly uniform under the contour levels, indicative of missing footprints from the wall-attached motions in the logarithmic region.

In summary, the SLSE results for streamwise velocity are quite similar to the incompressible case, suggesting weak compressibility effects on the linearized momentum equation under current flow conditions. By introducing μ_t and κ_t, the spectral linear
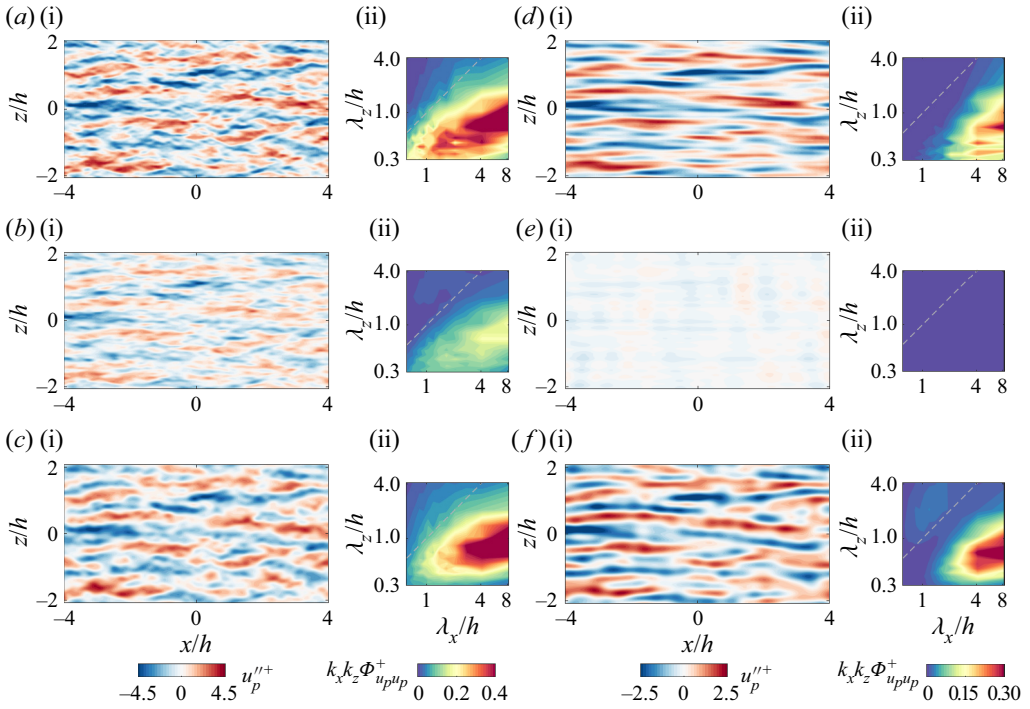
Figure 9. Estimated instantaneous $u_p''^+$ and the pre-multiplied 2-D spectra at $(a–c)$ $y_p^* = 70$ and $(d–f)$ $y_p^* = 10$ using the snapshot at $y_m^* = 107$ and the kernel function from the (a,d) DNS data and models of (b,e) LNS and (c,f) eLNS.

coherence and amplitude ratio of $\hat{u}''$ between different heights can be well captured by the linear models (eLNS), though the structures of small λ_z can be somewhat underestimated. This agreement gives us confidence to perform a parameter study for the velocity fluctuations in § 6. Instead of collecting large amounts of time-resolved measurements or simulations, the kernel function of velocity can be obtained using the eLNS model if one only has a mean flow. Then SLSE can be performed based on one snapshot of the velocity field.

5.3. *Estimation for temperature*

The SLSE results for temperature fluctuations are investigated in a similar style to § 5.2. In contrast to the velocity counterparts, the features of γ_{TT}^2 and $H_{L,TT}$ were rarely reported in previous studies, so the implications from DNS are discussed first.

The γ_{TT}^2 and $A_{pm,TT}$ from DNS are plotted in panels $(a−c)$ in figures 10 and 11 at $y_p^* = 70$, 40 and 10. The distribution of γ_{TT}^2 is very similar to γ_{uu}^2. In particular, figure 10(c) is nearly indistinguishable from figure 7(c) at $y_p^* = 10$. An important implication is that in the buffer layer, in addition to the nearly perfect correlation between u'' and T'' (see $R_{u''T''}$ and figure 6), the spectral coherence with the measurement (γ_{uu}^2 and γ_{TT}^2) are basically identical for $\hat{u}''$ and $\hat{T}''$, which benefits the compressible turbulence modelling. Moreover, γ_{TT}^2 is no lower than γ_{uu}^2 at the three y_p^* displayed, and is even higher in some regions with $\lambda_x < \lambda_z$. Therefore, the wall-normal spectral coherence of the temperature fluctuation is at least not weaker than the streamwise velocity. Intense inner–outer interaction is anticipated, and
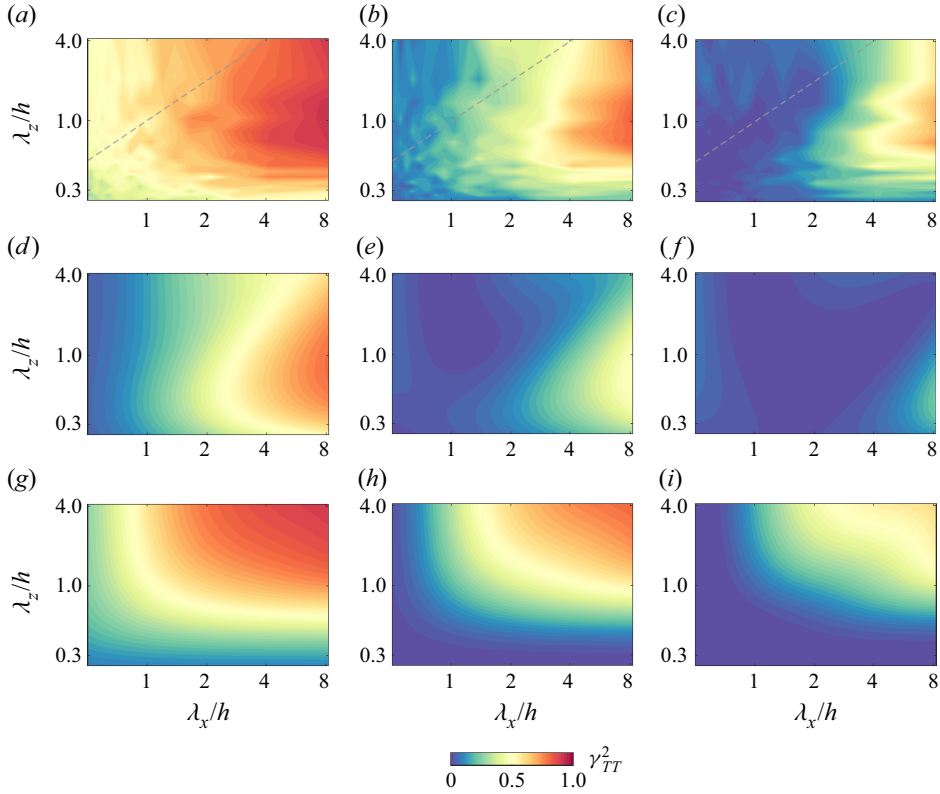
973 A36-24

Figure 10. Contours of 2-D LCS for T'' ($y_m^* = 107$) at (a,d,g) $y_p^* = 70$, (b,e,h) $y_p^* = 40$ and (c,f,i) $y_p^* = 10$. Panels $(a-c)$ are from the DNS data, $(d-f)$ are from the LNS model and $(g-i)$ are from the eLNS model.

the view is supported that T'' is also a wall-attached quantity (Cheng & Fu 2023a). The peaks of γ_{uu}^2 and γ_{TT}^2 are all located at $\lambda_z \approx h$ at different y_p^*, different from the impression from figure 6 that T'' tends to be more isotropic as y^* rises. High values of $A_{pm,TT}$ appear at $\lambda_z < 0.5h$, the same as that for $A_{pm,uu}$. The maximum $A_{pm,TT}$ exceeds six at $y_p^* = 10$ (figure 11c), which means that $\langle|\hat{T}_p''|^2\rangle$ with small λ_z increases rapidly towards the wall with respect to $\langle|\hat{T}_m''|^2\rangle$, due to local large temperature gradients.

The linear model results for T'' are discussed below. In general, the LNS model underestimates γ_{TT}^2 and $A_{pm,TT}$ at all y_p^* selected, the same as that for u''. The $A_{pm,TT}$ in figures 11(e) and 11(f) are less than unity in most regions, so the $\hat{T}''$ predicted is more localized with insufficient wall-normal connection. Nevertheless, the feature of λ_x preference over λ_z for γ_{TT}^2 is captured in the LNS model, and γ_{TT}^2 peaks at $\lambda_z \approx h$. The behaviour of the eLNS model, however, is quite different from those for u''. The γ_{TT}^2 in figures 10(g)–10(i) differs considerably from the DNS data, nearly isotropic in terms of λ_x and λ_z. Also, $A_{pm,TT}$ at all y_p^* is underestimated. Thereby, the eLNS model fails to give agreeable results with DNS for estimating temperature fluctuations. Revisiting the assumptions in § 3.2, (3.8a) treats T'' in an isotropic way, which may be responsible for the isotropic behaviour of γ_{TT}^2 in the eLNS model. Nevertheless, our numerical tests show that using (3.8b) instead does not improve obviously the results, though some degree of anisotropy is introduced. The discussion in § 4 suggests that acoustic and entropy components are significant in the eLNS model, but no supporting signs are observed
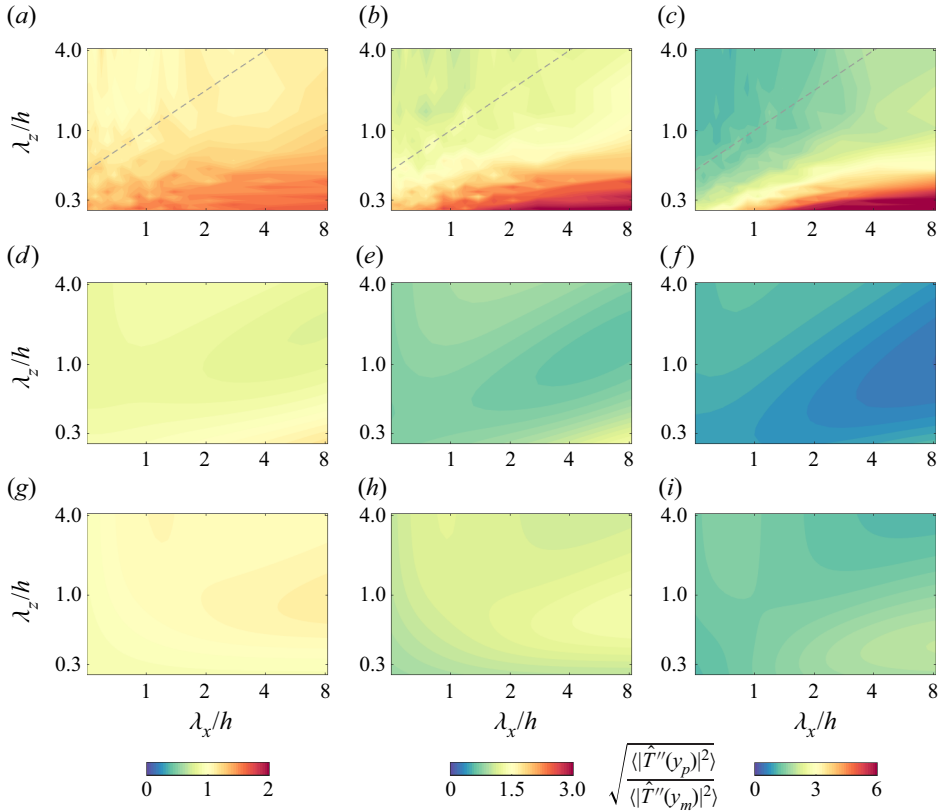
Figure 11. Contours of the amplitude ratio for T'' ($A_{pm,TT}$, $y_m^* = 107$) at (a,d,g) $y_p^* = 70$, (b,e,h) $y_p^* = 40$ and (c,f,i) $y_p^* = 10$. Panels $(a–c)$ are from the DNS data, $(d–f)$ are from the LNS model and $(g–i)$ are from the eLNS model.

from the displayed DNS data. Therefore, we check the eLNS results below for possible explanations of the differences.

5.4. *Cospectrum decomposition*

To figure out the difference between the eLNS and DNS results, $\boldsymbol{\Phi}$ is scrutinized. As discussed in §4, multiple branches of modes are present. One way to identify different mechanisms is to conduct a mode decomposition for $\boldsymbol{\Phi}$, known as the Karhunen–Loéve or proper orthogonal decomposition (POD). The eigenvalue problem is constructed as $\boldsymbol{\Phi}\check{q}''_j = \theta_j \check{q}''_j$, where θ_j is the eigenvalue, and the matrix–vector multiplication is defined in terms of the energy norm. Note that the symbol $\check{q}''_j$ is reused to represent the eigenfunctions for clarity, though the physical meaning is not identical to that in §4. Since $\boldsymbol{\Phi}$ is Hermite, θ_j is real. Also, $\check{q}''_j$ satisfies the orthogonal relation $(\check{q}''_i, \check{q}''_j)_E = E_b \delta_{ij}$ (E_b is the energy dimension). Different from (4.1), θ_j measures the energy of the jth POD mode ($\check{q}''_j$) and $\sum_j \theta_j = V$. If the pairs $(\theta_j, \check{q}''_j)$ are sorted in the descending order of θ_j, then $\check{q}''_1$ represents the leading energy-containing structure of the response.

The response with $\lambda_x = 8h$, $\lambda_z = 2h$ is considered first using the eLNS model, close to the maximum γ_{uu}^2 and γ_{TT}^2. Note that $\boldsymbol{\Phi}$ discussed below is the solution of (3.15), not (5.1).
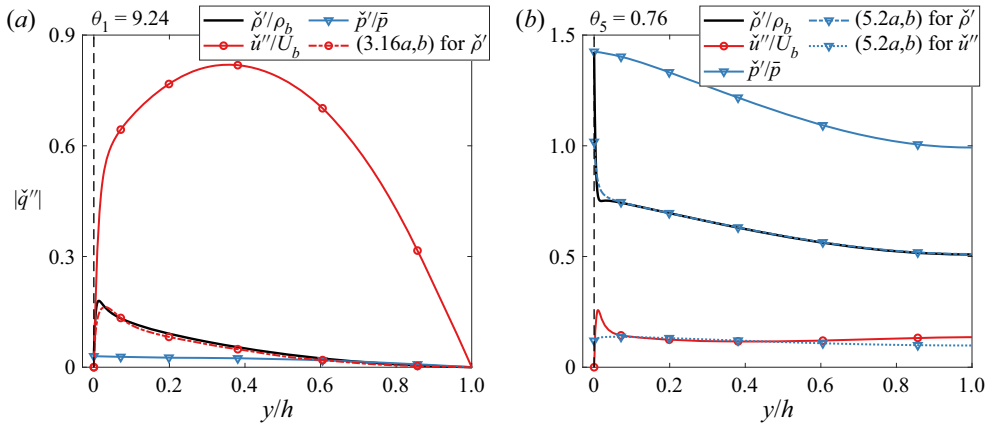
973 A36-26

Figure 12. Profiles of different components of the cospectrum POD modes in the eLNS model ($\lambda_x = 8h$, $\lambda_z = 2h$): (a) the most energetic mode (θ_1) and (b) the fifth most energetic mode (θ_5). Equations (3.16a,b) and (5.2a,b) are used to approximate other components based on $\check{u}''$ (for (a)) and $\check{p}'$ (for (b)).

After POD, at least two types of modes are identified, resulting from the different branches in §4. The most energetic mode $\check{q}_1''$ is shown in figure 12(a), where $\check{u}''$ is the largest component. Meanwhile, $\check{\rho}'$ and $\check{T}''$ (not shown) can be well approximated by (3.16a,b) and $\check{u}''$, analogous to figure 2. This demonstrates that $\check{\rho}'$ and $\check{T}''$ of this mode are dominated by advection, and $\check{q}_1''$ is in line with the trends in DNS. Therefore, this mode is termed an advection mode, which can be considered as a subset of the vortical modes. The dilatation of the advection mode is tiny, and $\check{p}'/\bar{p}$ is also small, thus analogous to the incompressible counterpart. Meanwhile, the advection mode takes the form of streamwise-elongated velocity ($\check{u}''$), density and temperature streaks forced by streamwise vortices ($\check{v}''$, $\check{w}''$), as observed in figure 6 and reported in previous experimental, DNS and linear-model results (Coleman *et al.* 1995; Williams *et al.* 2018; Chen *et al.* 2023). A 3-D view of this mode will be shown later. Modes $\check{q}_2''$, $\check{q}_3''$ and $\check{q}_4''$ have similar features to $\check{q}_1''$, but $\check{q}_5''$ is different. As shown in figure 12(b) for $\check{q}_5''$, $\check{p}'$ and $\check{\rho}'$ are much larger than $\check{u}''$, and $\check{\rho}'$ is in high amplitude at the wall, so this mode experiences strong dilatation. This mode is of an acoustic nature, as discussed in §4.1. To prove this, the analytical eigenfunction of the acoustic mode in the free stream is used (see Appendix B), leading to the following relations:

$$\frac{\check{\rho}'}{\bar{\rho}} = \frac{\check{p}'}{\gamma_0 \bar{p}}, \quad \frac{\check{u}''}{a} = \frac{k_x}{\sqrt{k_x^2 + k_y^2 + k_z^2}} \frac{\check{p}'}{\gamma_0 \bar{p}}, \qquad (5.2a,b)$$

where a is the speed of sound. Equation (5.2a,b) is examined in figure 12(b) with $k_y = 0$. Even though (5.2a,b) is derived based on a uniform mean flow, remarkable agreement is observed for both $\check{\rho}'$ and $\check{u}''$, confirming that $\check{q}_5''$ is of an acoustic nature except in the near-wall region. The large $\check{\rho}'$ at the wall is due to the prescribed boundary condition $\check{T}_w'' = 0$. Furthermore, a series of acoustic modes exist with different k_y, as shown in figure 13. These modes with $k_y \neq 0$ strongly oscillate in the interior region with (5.2a,b) also satisfied, and the maximum amplitudes of $\check{\rho}'$ and $\check{p}'$ remain nearly constants. The θ_j of these modes are labelled in figures 12 and 13, non-dimensionalized by h/U_b. The energy ratio of the most energetic acoustic and advection modes is 8.2 % (θ_5/θ_1), so these acoustic modes have non-negligible contributions to $\boldsymbol{\Phi}$. In comparison, the same ratio in the LNS case is only 0.06 %. Therefore, the conclusion in §4 is supported since the
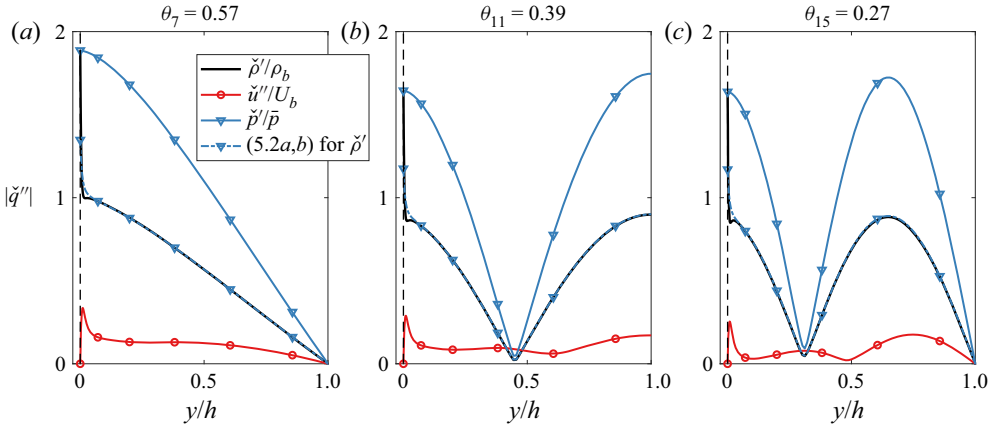
973 A36-27

Figure 13. Profiles of different components of the cospectrum POD modes in the eLNS model ($\lambda_x = 8h$, $\lambda_z = 2h$): the (a) seventh, (b) eleventh and (c) fifteenth energetic modes. Equation (5.2a,b) is used to approximate other components based on $\check{p}'$.

acoustic components are negligible for the response in the LNS case, but non-negligible in the eLNS case. Moreover, no counterparts to the entropy modes are found in at least the top thirty most energetic modes in both the LNS and eLNS cases, suggesting their relatively small contribution than the acoustic components at this length scale.

Considering § 4, and observing the great similarities between u'' and T'' in §§ 5.2 and 5.3, it is conjectured that the significant role of acoustic and entropy components to the fluctuation growth in the eLNS model is an intrinsic defect introduced by the turbulence modelling. To verify this, $\boldsymbol{\Phi}$ is decomposed to exclude the contributions of acoustic and entropy modes, denoted as $\boldsymbol{\Phi}_{ae}$, and the remaining part is $\boldsymbol{\Phi}_{nae}$. The eigenvalue problem above does not allow a strict decomposition as $\boldsymbol{\Phi} = \boldsymbol{\Phi}_{ae} + \boldsymbol{\Phi}_{nae}$, so the singular value decomposition is deployed instead, taking the form of

$$\boldsymbol{\Phi} = \sum_j \sigma_j \check{\boldsymbol{\psi}}_j \check{\boldsymbol{\phi}}_j^H = \underbrace{\sum_{j \in ae} \sigma_j \check{\boldsymbol{\psi}}_j \check{\boldsymbol{\phi}}_j^H}_{\boldsymbol{\Phi}_{ae}} + \underbrace{\sum_{j \in nae} \sigma_j \check{\boldsymbol{\psi}}_j \check{\boldsymbol{\phi}}_j^H}_{\boldsymbol{\Phi}_{nae}}, \qquad (5.4)$$

where σ_j is the singular value, and $\check{\boldsymbol{\psi}}_j$ and $\check{\boldsymbol{\phi}}_j$ are the decomposition modes. As $\boldsymbol{\Phi}$ is Hermite, $\check{\boldsymbol{\psi}}_j = \check{\boldsymbol{\phi}}_j$; σ_j and $\check{\boldsymbol{\psi}}_j$ have analogous behaviours to θ_j and $\check{q}_j''$, hence are not elaborated for conciseness. The same criteria as in § 4 are deployed to identify the acoustic and entropy modes, based on their eigenfunctions (see figure 4). It is worth mentioning the difference of the decompositions in figure 5 and (5.4). The former is to exclude the acoustic (or entropy) eigenmodes of the linear operator before solving the response, while the latter is a posterior decomposition of the response with all eigenmodes included. The two strategies are not equivalent, and the latter is adopted here because the acoustic and entropy modes are not fully decoupled with the vortical modes (see § 4), especially in the near-wall region.

The cospectrum decomposition results using (5.4) are displayed in figure 14, still with $\lambda_x = 8h$, $\lambda_z = 2h$. They are normalized by the maximum of $\langle \hat{u}'' \hat{u}''^\dagger \rangle$. Interestingly, $\langle \hat{\rho}' \hat{\rho}'^\dagger \rangle$, $\langle \hat{u}'' \hat{u}''^\dagger \rangle$ and $\langle \hat{u}'' \hat{T}''^\dagger \rangle$ have clear attributions, suggesting a rather 'perfect' decomposition. Here, 'perfect' means that we can clearly identify which physical process is responsible for the generation of different components. Specifically, nearly all $\langle \hat{\rho}' \hat{\rho}'^\dagger \rangle$ are contributed
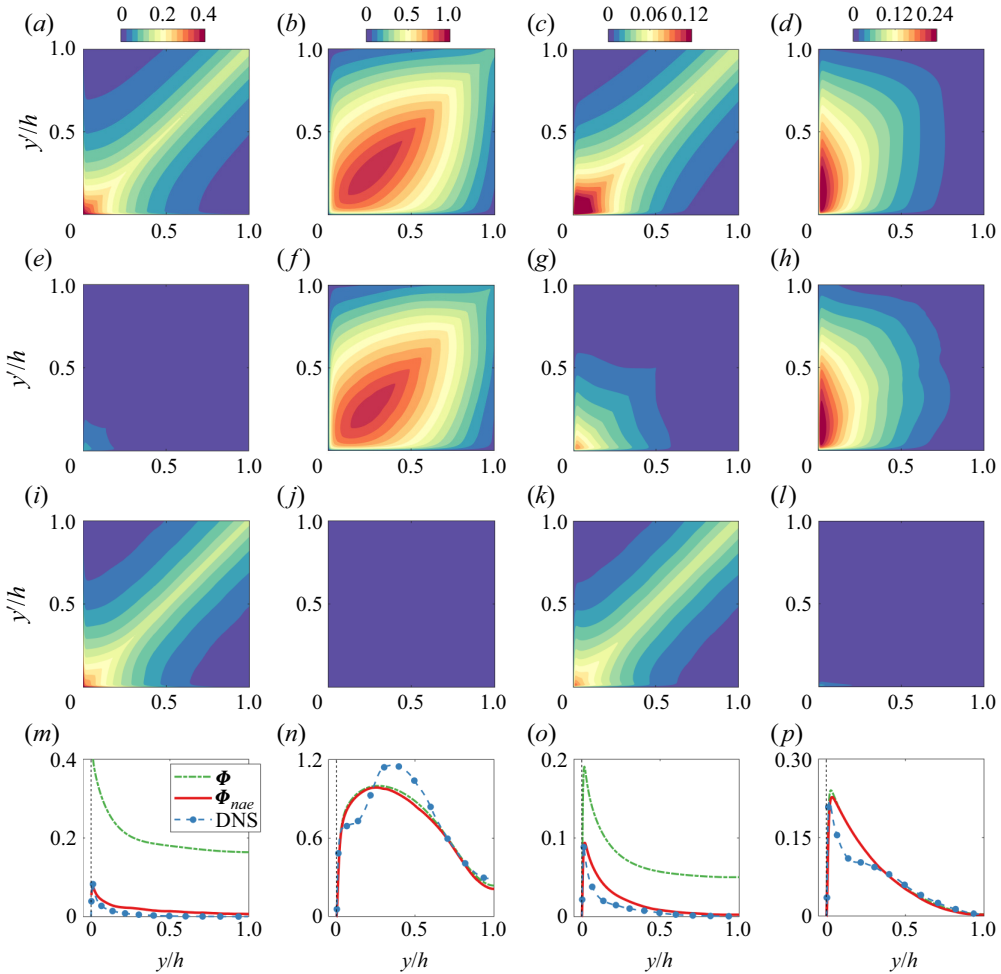
973 A36-28

Figure 14. Cospectra of different components in the eLNS model ($\lambda_x = 8h$, $\lambda_z = 2h$): (a,e,i,m) $\langle \hat{\rho}' \hat{\rho}'^{\dagger} \rangle$, ($b,f,j,n$) $\langle \hat{u}'' \hat{u}''^{\dagger} \rangle$, ($c,g,k,o$) $\langle \hat{T}'' \hat{T}''^{\dagger} \rangle$ and (d,h,l,p) $|\langle \hat{u}'' \hat{T}''^{\dagger} \rangle|$. They are non-dimensionalized by ρ_b, U_b and T_w accordingly. Panels (a–d) are the original results containing all modes, (e–h) are from $\boldsymbol{\Phi}_{nae}$ and (i–l) are from $\boldsymbol{\Phi}_{ae}$. The coordinates y and y' are for the two variables of cospectra, respectively (see (2.7)). Panels (m–p) are the comparisons with $\boldsymbol{\Phi}_{DNS}$ at $y' = y$.

by $\boldsymbol{\Phi}_{ae}$, while the contribution of $\boldsymbol{\Phi}_{nae}$ is tiny (figures 14e and 14i). From figure 12(a), the latter part can be approximated by u'' and the mean flow gradients, representing the advection effect. In contrast, $\langle \hat{u}'' \hat{u}''^{\dagger} \rangle$ and $\langle \hat{u}'' \hat{T}''^{\dagger} \rangle$ are mostly contributed by $\boldsymbol{\Phi}_{nae}$, nearly unaffected by the acoustic and entropy components. Thereby, the eLNS results for u'' in § 5.2 basically agree with DNS, as in the incompressible case. Also, it is suggested that the u''–u'' and u''–T'' couplings are dominated by advection and other vortical motions, while the acoustic- and entropy-induced motions have little coherence for the couplings. For $\langle \hat{T}'' \hat{T}''^{\dagger} \rangle$, $\boldsymbol{\Phi}_{nae}$ and $\boldsymbol{\Phi}_{ae}$ have nearly equal contributions. The former is more concentrated towards the wall, represented by (3.16a,b), while the latter extends to the channel centre populating neutral acoustic and entropy waves. To further justify the decomposition, the normalized $\boldsymbol{\Phi}$ from DNS is also computed. Since we are mainly concerned with the relative amplitudes of $\boldsymbol{\Phi}_{nae}$ and $\boldsymbol{\Phi}_{ae}$, only the $\boldsymbol{\Phi}$ with $y = y'$ are extracted for comparison,

as shown in figures 14(*m*)–14(*p*). For $\langle \hat{u}''\hat{u}''^{\dagger}\rangle$ and $\langle \hat{u}''\hat{T}''^{\dagger}\rangle$, $\boldsymbol{\Phi}$ and $\boldsymbol{\Phi}_{nae}$ are close to each other and they basically follow $\boldsymbol{\Phi}_{DNS}$, though differences in shapes are observable. The $\boldsymbol{\Phi}$ in the eLNS model varies more mildly than the DNS data, possibly due to using a smooth μ_t. For $\langle \hat{\rho}'\hat{\rho}'^{\dagger}\rangle$ and $\langle \hat{T}''\hat{T}''^{\dagger}\rangle$, however, $\boldsymbol{\Phi}$ is several times higher than $\boldsymbol{\Phi}_{DNS}$, exhibiting large values around the centreline. After the decomposition, $\boldsymbol{\Phi}_{nae}$ is much closer to $\boldsymbol{\Phi}_{DNS}$, also tending to diminish towards the channel centre. Thereby, we can conclude that the acoustic and entropy components $\boldsymbol{\Phi}_{ae}$ in the eLNS model barely exist in the DNS data. In short, in the eLNS model, $\langle \hat{u}''\hat{u}''^{\dagger}\rangle$ and $\langle \hat{u}''\hat{T}''^{\dagger}\rangle$ remain little influenced by the acoustic and entropy components, while $\langle \hat{\rho}'\hat{\rho}'^{\dagger}\rangle$ and $\langle \hat{T}''\hat{T}''^{\dagger}\rangle$ are largely affected, which can be responsible for the deviation of $H_{L,TT}$ in § 5.3. For improvement, we use $\boldsymbol{\Phi}_{nae}$ in the following to estimate temperature and also the velocity–temperature coupling. The results are denoted as eLNS-CD ('CD' for cospectrum decomposition).

Before presenting the eLNS-CD results, we need to examine whether the dominant advection mode in figure 12 is a universal feature at different length scales. The scales $(\lambda_x, \lambda_z) = (8h, 0.3h)$, $(0.3h, 2h)$ and $(0.3h, 0.3h)$ are considered in addition to $(8h, 2h)$ in figure 12, covering the large and small streamwise/spanwise scales studied in § 5.3. The velocity and temperature components of the most energetic modes at these scales are plotted in figure 15. Their 3-D structures are depicted in figure 16, where $u''_{(k_x, k_z)} = \breve{u}''_{(k_x, k_z)}(y) \exp[\mathrm{i}(k_x x + k_z z)]$ (from (2.3)). The energetic large-scale mode $(8h, 2h)$ wanders across different layers, crucial for the inner–outer interaction as discussed above. This type of mode is also characterized by geometrically self-similar hierarchies (McKeon 2019). The mode $(8h, 0.3h)$ is also an advection mode as in figure 12(*a*), exhibiting streamwise-elongated streaky motions very close to the wall. The peaks of $\breve{u}''$ and $\breve{T}''$ are at $y^* = 14$ and 11, respectively, within the buffer layer. Also, $\breve{\rho}'$ and $\breve{T}''$ result primarily from the advection process, well approximated by (3.16*a*,*b*). In comparison, the mode $(0.3h, 2h)$ is spanwise elongated (since $\lambda_z > \lambda_x$) with large amplitudes of $\breve{v}''$ and $\breve{w}''$. This mode is not dominated by streamwise advection, but also results from vortical modes since the thermodynamic components are small. For the mode $(0.3h, 0.3h)$ in figures 15(*c*) and 16(*d*), $\breve{v}''$ is the largest component and $\breve{u}'' \sim \breve{w}''$ as $\lambda_x \sim \lambda_z$. This mode is mostly amplified around $y \approx 0.5h$, and its oblique structure can be associated with the spanwise meandering of large-scale motions (Hutchins & Marusic 2007; Abe *et al.* 2018). Meanwhile, its $\breve{T}''$ component is in low amplitude, much lower than the approximation by (3.16*a*,*b*). In short, with the decrease of λ_x, the most energetic structure changes gradually from the motions dominated by streamwise advection to spanwise elongation. Consequently, the cospectrum decomposition at small λ_x may not be as 'perfect' as in figure 14. From §§ 5.2 and 5.3, the structures with smaller λ_x tend to have weaker coherence for the velocity and temperature fluctuations between different heights, so they can be of secondary importance for SLSE.

The γ^2_{TT} and $A_{pm,TT}$ from the eLNS-CD model are displayed in figures 17 and 18 at the same y^*_m and y^*_p as in § 5.3. The DNS results in figures 10 and 11 are re-plotted for easier comparison. The cospectrum decomposition requires categorization of the POD modes, so the eLNS-CD results are not as smooth as those by eLNS, as discussed for figures 5(*e*) and 15. As can be seen, after removing the acoustic and entropy components, γ^2_{TT} and $A_{pm,TT}$ are in good agreement with DNS. To be specific, γ^2_{TT} from eLNS-CD is not as isotropic as that in figure 10 (eLNS results), and the scale selection in terms of λ_z is captured, so γ^2_{TT} does not monotonically increase with λ_z. Meanwhile, the high $A_{pm,TT}$ at $\lambda_z < 0.5h$ is correctly reflected, showing a prominent improvement over figures 11(*g*)–11(*i*).
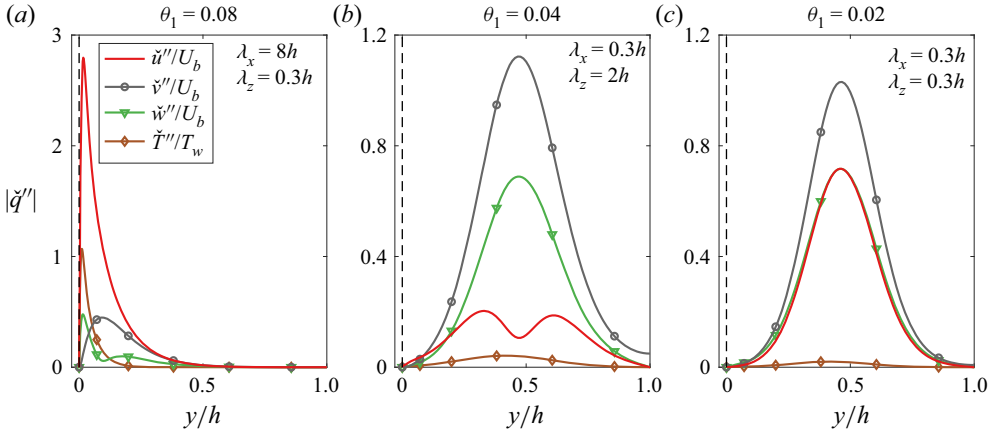
973 A36-30

Figure 15. Different components of the most energetic POD modes (θ_1) for the eLNS cospectrum at different length scales (λ_x, λ_z): (a) (8h, 0.3h), (b) (0.3h, 2h) and (c) (0.3h, 0.3h).
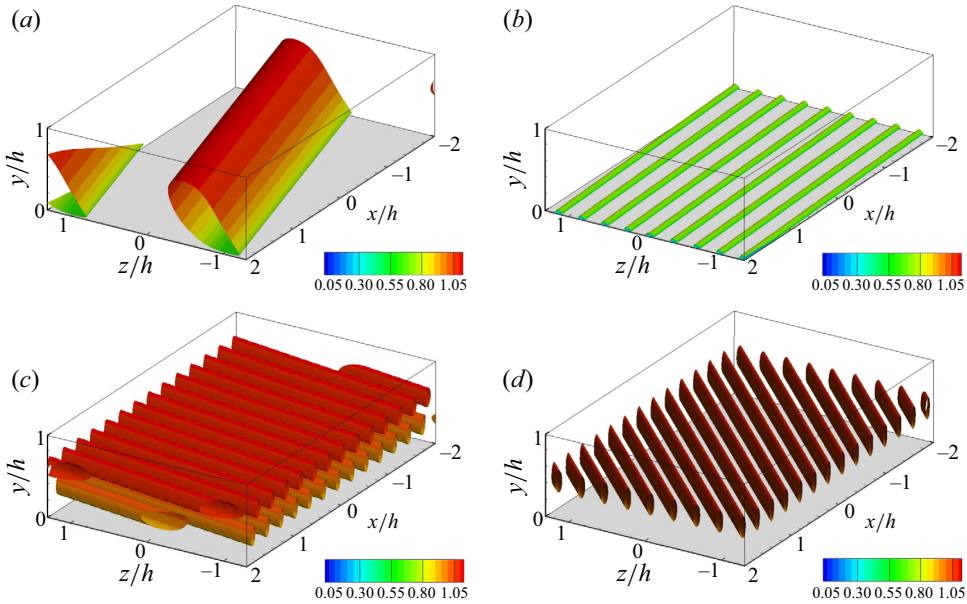

Figure 16. Isosurface $u''_{(k_x,k_z)}/max|u''_{(k_x,k_z)}| = 0.6$ of the most energetic mode of the eLNS cospectrum for (λ_x, λ_z) of (a) (8h, 2h), (b) (8h, 0.3h), (c) (0.3h, 2h) and (d) (0.3h, 0.3h), flooded by the mean velocity $\tilde{u}/U_b$.

Finally, the instantaneous T'' at y_m^* is utilized to estimate the coherent temperature structures (T_p'') at different y_p^*. The estimated 2-D spectra $\Phi^+_{T_p T_p}(y_p)$ as in (5.1) are also computed. First, the estimations using $H_{L,TT}$ from DNS are depicted in figures 19(a) and 19(d). Compared with figure 9(a), relatively more energy resides at $\lambda_x \sim h$, contributing to the more isotropic pattern of temperature than the streamwise velocity counterpart. The estimated T_p'' at $y_p^* = 10$ is dominated by streamwise streaks and resembles a lot the velocity counterpart in figure 9(d) except for smaller amplitudes. Similar to figure 9, the LNS model severely underestimates the amplitude of T_p'' at nearly all scales, especially close to the wall where the two plots in figure 19(e) are nearly uniform. In comparison,
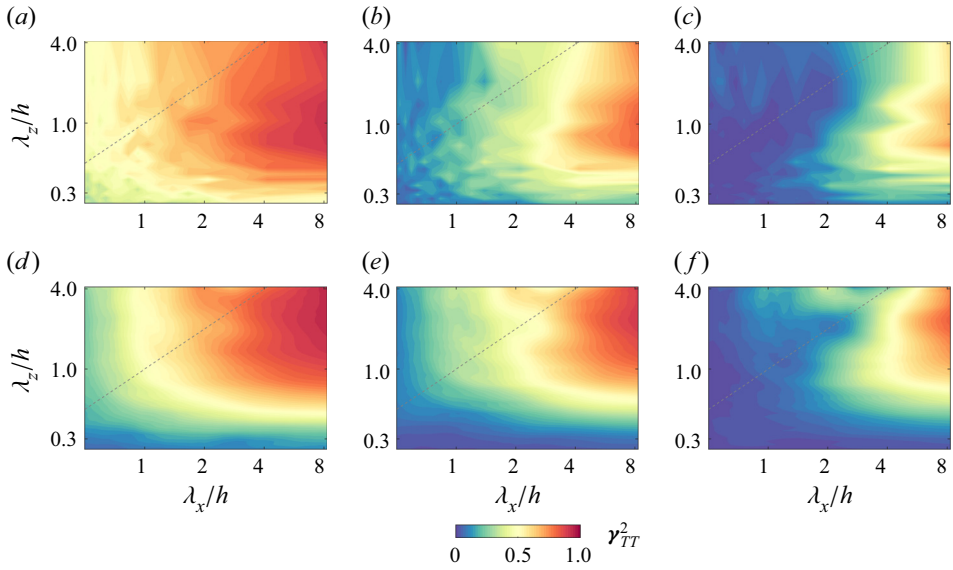
Figure 17. Contours of 2-D LCS for T'' ($y_m^* = 107$) at (a,d) $y_p^* = 70$, (b,e) $y_p^* = 40$ and (c,f) $y_p^* = 10$. Panels $(a-c)$ are from the DNS data and $(d-f)$ are from the eLNS model after the cospectrum decomposition (eLNS-CD). The dotted lines denote $\lambda_x = \lambda_z$.
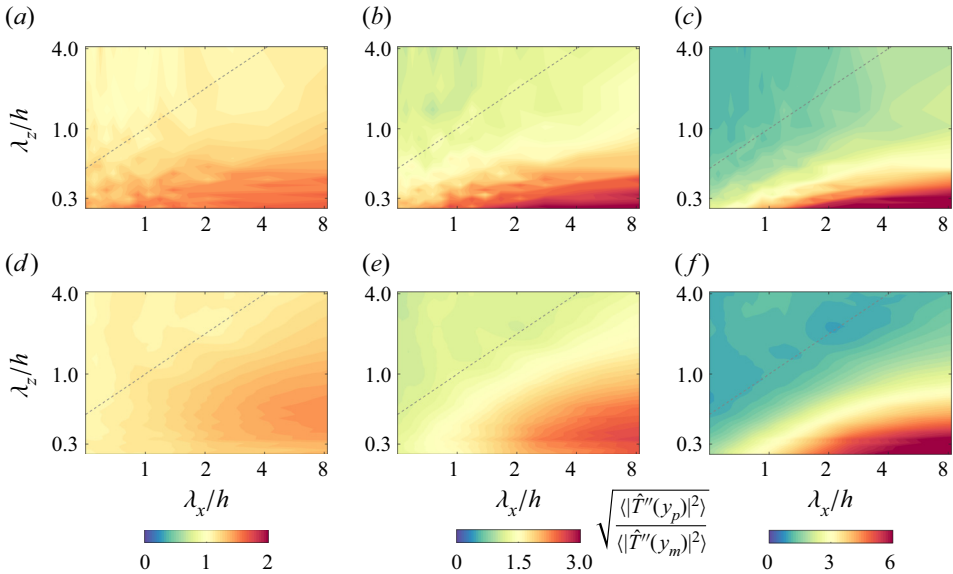

Figure 18. Contours of the amplitude ratio for T'' ($A_{pm,TT}$, $y_m^* = 107$) at (a,d) $y_p^* = 70$, (b,e) $y_p^* = 40$ and (c,f) $y_p^* = 10$. Panels $(a-c)$ are from the DNS data and $(d-f)$ are from the eLNS-CD model. The dotted lines denote $\lambda_x = \lambda_z$.

the eLNS-CD results exhibit significant improvements over the LNS and eLNS models, as expected from figures 17 and 18. The estimated large-scale structures ($\lambda_x \gtrsim 3h$) agree well with the DNS data, but the smaller-scale motions in figure 19(c) are obviously under-predicted due to the underestimated γ_{TT}^2 in figure 17(d) at small λ_x.
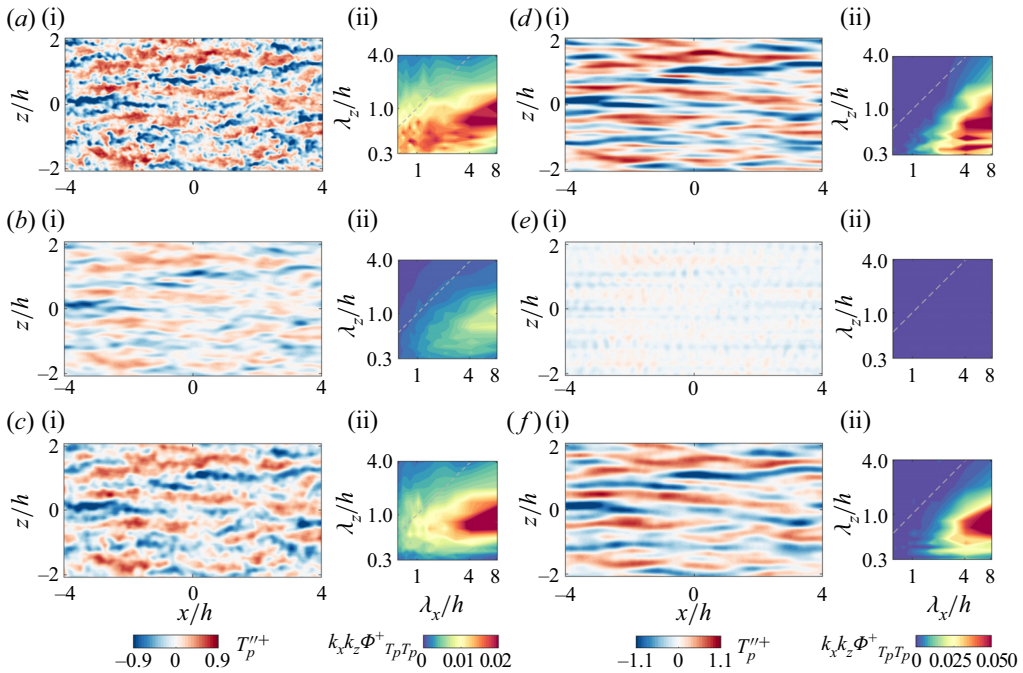
973 A36-32

Figure 19. Estimated instantaneous $T_p''^+$ and the pre-multiplied 2-D spectra at (a,b,c) $y_p^* = 70$ and (d,e,f) $y_p^* = 10$ using the snapshot at $y_m^* = 107$ and the kernel function from the (a,d) DNS data and models of (b,e) LNS and (c,f) eLNS-CD.

Therefore, the eLNS model can reflect reasonably the wall-normal coherence and amplitude variation of the temperature fluctuation, but it can be deteriorated by the overdamped vortical modes and thus relatively intensified acoustic and entropy components due to the changed mathematical properties of the linear operator. Through a procedure of cospectrum decomposition (eLNS-CD), the interference from the acoustic and entropy components can be removed to obtain SLSE results that basically agree with DNS data. Meanwhile, an important implication is that the coherence of temperature is dominated by the vortical components, including advection and other kinematically dominated motions, strongly analogous to the incompressible case. The compressibility effects, exerting influence through the acoustic and entropy components, are of secondary importance.

5.5. *Estimation for velocity–temperature coupling*

Cheng & Fu (2023a) show that SLSE can be designed to estimate the velocity–temperature coupling (§ 2.3). Here we provide the results from the linear models to examine whether γ_{uT}^2 and $H_{L,uT}$ can be reasonably predicted. First of all, γ_{uT}^2 and $A_{pm,uT} = (\langle|\hat{T}_p''|^2\rangle/\langle|\hat{u}_m''|^2\rangle)^{1/2}$ from DNS are displayed in figures 20(a)–20(c). Two types of y_m^* and y_p^* combinations are considered, namely $y_m^* = y_p^*$ and $y_m^* \neq y_p^*$. In the former case, the measured u'' is used for predicting the local T'' at the same height, while in the latter case, T'' at another height is predicted. In figure 20(a), $y_m^* = y_p^* = 14$ are both in the buffer layer, and u'' and T'' have close morphological connections (see § 5.1). Therefore, γ_{uT}^2 is larger than 0.6 in most length scales displayed, and the streamwise-elongated
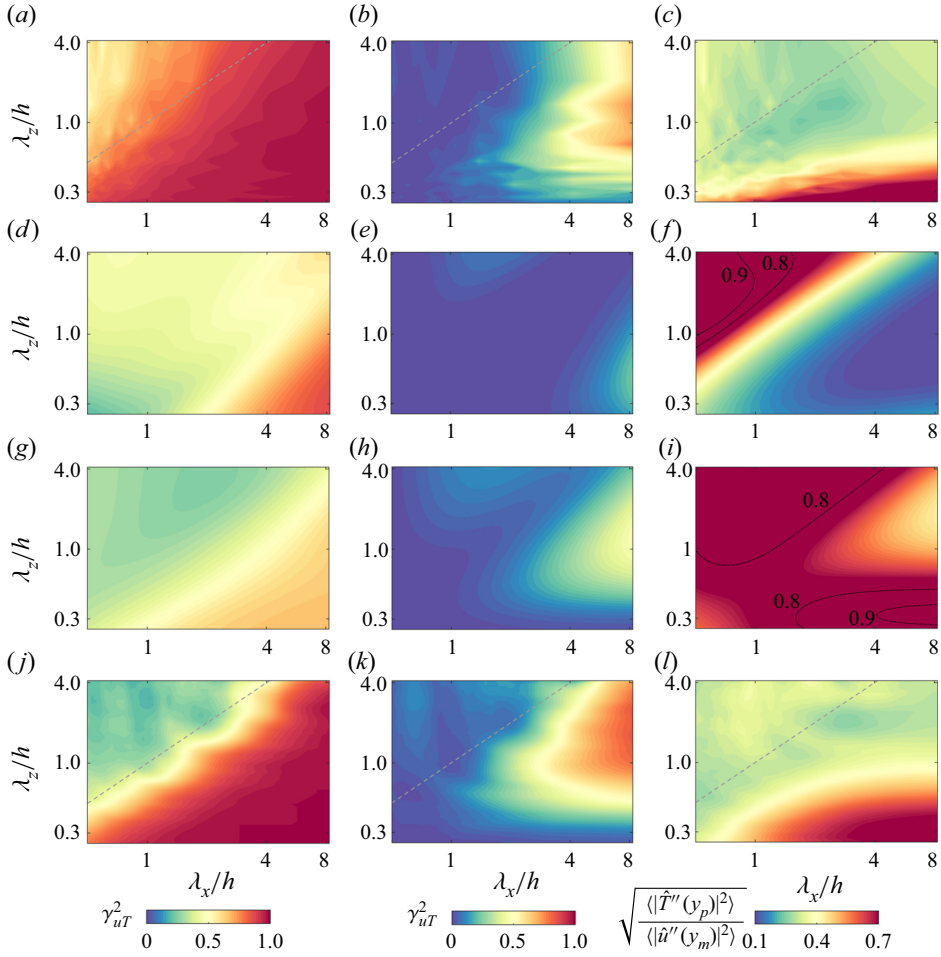
Figure 20. Contours of 2-D LCS and amplitude ratio for the u''–T'' coupling from the $(a$–$c)$ DNS data, and the models of $(d$–$f)$ LNS, $(g$–$i)$ eLNS and $(j$–$l)$ eLNS-CD. Panels (a,d,g,j) are at $y_m^* = y_p^* = 14$, and other panels are at $y_m^* = 107$, $y_p^* = 14$. Panels (c,f,i,l) are for the amplitude ratio $(\langle |\hat{T}''(y_p)|^2 \rangle / \langle |\hat{u}''(y_m)|^2 \rangle)^{1/2}$, and other panels are for γ_{uT}^2. The dotted lines denote $\lambda_x = \lambda_z$. The dash-dot lines in (f,i) are the contours in the saturating region.

streaky motions (larger λ_x and smaller λ_z) are more coherent in terms of the coupling. Meanwhile, $A_{pm,uT} \approx 0.35$ (non-dimensionalized by U_b, T_w) is nearly uniform at different scales (not shown), close to the mean flow coefficient between u''_{rms} and T''_{rms} in (3.16a,b). Figures 20(b) and 20(c) are for the case $y_m^* \neq y_p^*$, where $y_m^* = 107$ is at the centre of the logarithmic region and y_p^* is in the buffer layer. Here, γ_{uT}^2 and $A_{pm,uT}$ have similar distributions to those for u''–u'' and T''–T'', which is reasonable considering the strong analogies between γ_{uu}^2 and γ_{TT}^2, and $A_{pm,uu}$ and $A_{pm,TT}$.

From figure 20, γ_{uT}^2 and $A_{pm,uT}$ from LNS and eLNS considerably deviate from the DNS data. The γ_{uT}^2 at different y_m^* and y_p^* are underestimated in both models. In addition, $A_{pm,uT}$ in the LNS case is high for spanwise-elongated motions ($\lambda_z > \lambda_x$) but low for the streamwise-elongated ($\lambda_x > \lambda_z$), opposite to the DNS trend. Also, $A_{pm,uT}$ in the eLNS
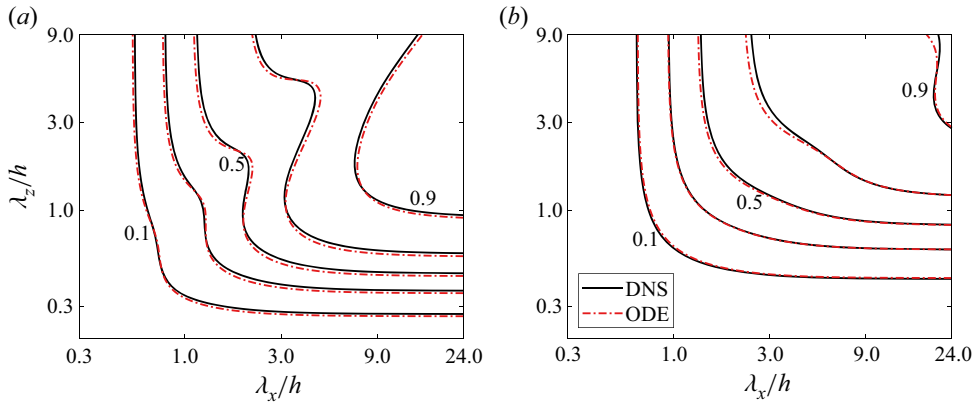
973 A36-34

Figure 21. Contours of (*a*) γ_{uu}^2 and (*b*) γ_{TT}^2 using the mean flows from DNS and the ODE-based solver, respectively. Here, y_m^* is fixed at 107, and $y_p^* = 40$. The levels displayed are 0.1, 0.3, 0.5, 0.7 and 0.9, as labelled.

case exhibits an overall higher value at nearly all λ_x and λ_z. From figure 14, $\langle \hat{u}''\hat{T}''^\dagger \rangle$ by eLNS is little affected by the acoustic and entropy components, but γ_{uT}^2 and $A_{pm,uT}$ are influenced since they are related to $\langle \hat{T}''\hat{T}''^\dagger \rangle$. After the cospectrum decomposition, the eLNS-CD results in figures 20(*j*)–20(*l*) are much closer to DNS. The scale dependence of γ_{uT}^2 and $A_{pm,uT}$ are correctly captured, for both $y_m^* = y_p^*$ and $y_m^* \neq y_p^*$ cases. Nevertheless, an obvious deviation is that γ_{uT}^2 for the spanwise-elongated motions is underestimated in figure 20(*j*). As discussed in figure 15(*b*), wall-normal and spanwise motions dominate at these scales, affecting the performance of the cospectrum decomposition. In summary, the eLNS model can be used to estimate the velocity–temperature coupling after the cospectrum decomposition (eLNS-CD). Analogous to the coherence of temperature, the coupling of the coherent velocity and temperature fluctuations is also dominated by advection and other vortical components, while the compressibility effects are of secondary importance. Thereby, the present results support and provide more proof for the conclusions of Cheng & Fu (2023*a*).

6. Parameter study

Observing the consistency between the DNS data and the linear models, a parameter study is performed to investigate the variations of γ^2 and A_{pm} with different Ma_b and Re_τ. As the compressible DNS database is very limited, the ODE solver in § 2.2 is utilized to obtain the mean flows of varying Ma_b and Re_τ. First, we need to confirm that the SLSE results predicted by the ODE-based mean flow are as reliable as those using the DNS mean flow. The benchmark case is calculated, and the comparisons of γ_{uu}^2 and γ_{TT}^2 are shown in figure 21 using the two mean flows. The y_m^* and y_p^* are the same as those in § 5, with $y_p^* = 40$ in the logarithmic layer. Note that the result comparisons for other y_p^* are similar and thus not shown for conciseness. For an overall comparison, the ranges of λ_x and λ_z are much larger than those in § 5, without the limitation of the DNS computational domain. Only the eLNS model is selected, and the LNS model is not considered due to the relatively large deviation. Basically, γ_{uu}^2 and γ_{TT}^2 using the DNS and ODE mean flows agree with each other within the length scales displayed, demonstrating the reliability of the ODE solver in predicting SLSE results.

Ma_b	$Re_{\tau,c}^*$	Re_τ	Re_b	$\tilde{T}_c/T_w$	y_m^+ ($y_m^* = 107$)	y_p^+ ($y_p^* = 70$)	y_p^+ ($y_p^* = 10$)
0.3	780	782	15000	1.00	109	71.2	10.1
1.5	780	1165	19400	1.37	156	101	12.9
3.0	780	2360	29700	2.53	309	198	21.9
4.0	780	3620	37900	3.72	471	301	31.4

Table 1. Parameters for channel flow cases with different Ma_b but the same $Re_{\tau,c}^*$.

Semi-local units have been extensively proven to be capable of collapsing various turbulent quantities to their incompressible counterparts, such as the mean velocity profile (Griffin *et al.* 2021), Reynolds stress (Huang *et al.* 1995), the spanwise spacing of near-wall streaks (Morinishi *et al.* 2004), kinetic energy budget (Duan *et al.* 2010) and streamwise inclination angles (Bai, Cheng & Fu 2023). One interesting point is to examine whether semi-local units collapse the 2-D LCS and amplitude ratio. This is conducive to the modelling of inner–outer interaction for compressible flows. In addition to the benchmark case, three more cases are considered, with varying Ma_b but the same $Re_{\tau,c}^*$. Their computational parameters are listed in table 1. The $Ma_b = 0.3$ case is close to the incompressible condition with nearly uniform $\bar{\rho}$ and $\tilde{T}$, and the fourth case has a high Ma_b of 4.

With Ma_b increased, Re_τ and Re_b grow rapidly due to the stronger variation of the thermodynamic properties. These two Reynolds numbers are positively correlated with the required grid points for DNS, so the computational cost dramatically increases with the rise of Ma_b, which is largely responsible for the limited DNS database for compressible channel flows.

For different cases, y_m^* and y_p^* are kept the same, though the corresponding y_m^+ and y_p^+ increase by over three times with Ma_b lifted. Meanwhile, the streamwise and spanwise wavelengths of fluctuations are all expressed in the outer scale, i.e. λ_x/h and λ_z/h. The contours of γ_{uu}^2 and $A_{pm,uu}$ are depicted in figure 22 at $y_p^* = 70$ and 10. The γ_{uu}^2 at $y_p^* = 70$ varies slightly with Ma_b increased from 0.3 to 4.0, which means that the compressibility effects on the spectral coherence of streamwise velocity in the logarithmic region can be scaled using semi-local units, supporting Morkovin's hypothesis. When y_p^* is down to 10 in the buffer layer, the differences of γ_{uu}^2 among cases are more obvious, especially at large λ_z. Nevertheless, there is still good collapse for streamwise-elongated streaky motions with $\lambda_x \gtrsim 5h$ and $\lambda_z \lesssim 0.5h$. In figures 22(*b*) and 22(*d*), the region $A_{pm,uu} > 1$, i.e. $\langle|\hat{u}_p''|^2\rangle > \langle|\hat{u}_m''|^2\rangle$, is mainly concentrated at $\lambda_x > \lambda_z$, little influenced by Ma_b. In contrast, $A_{pm,uu}$ at $\lambda_x < \lambda_z$ exhibits Ma_b dependence, where γ_{uu}^2 is low and the dominant POD mode for the cospectrum is not an advection mode (see § 5.4). In summary, γ_{uu}^2 and $A_{pm,uu}$ of the streamwise-elongated ($\lambda_x > \lambda_z$) structures with high coherence exhibit good Ma_b independence within and below the logarithmic region when using semi-local units. These structures have high $A_{pm,uu}$, so they are pronounced and tend to be dominant for the estimated $u''(y_p^*)$, beneficial for constructing the compressible IOIM. In contrast, the spanwise-elongated structures with $\lambda_x < \lambda_z$ are more influenced by Ma_b. They tend to be of secondary importance for SLSE because of the relatively low γ_{uu}^2 and $A_{pm,uu}$.

The parameter study regarding temperature is not conducted for two reasons. First, heat transfer needs to be included in the incompressible case for reference (Antonia *et al.* 2009), but such cases are not currently available in our dataset. Second, the conclusions presented
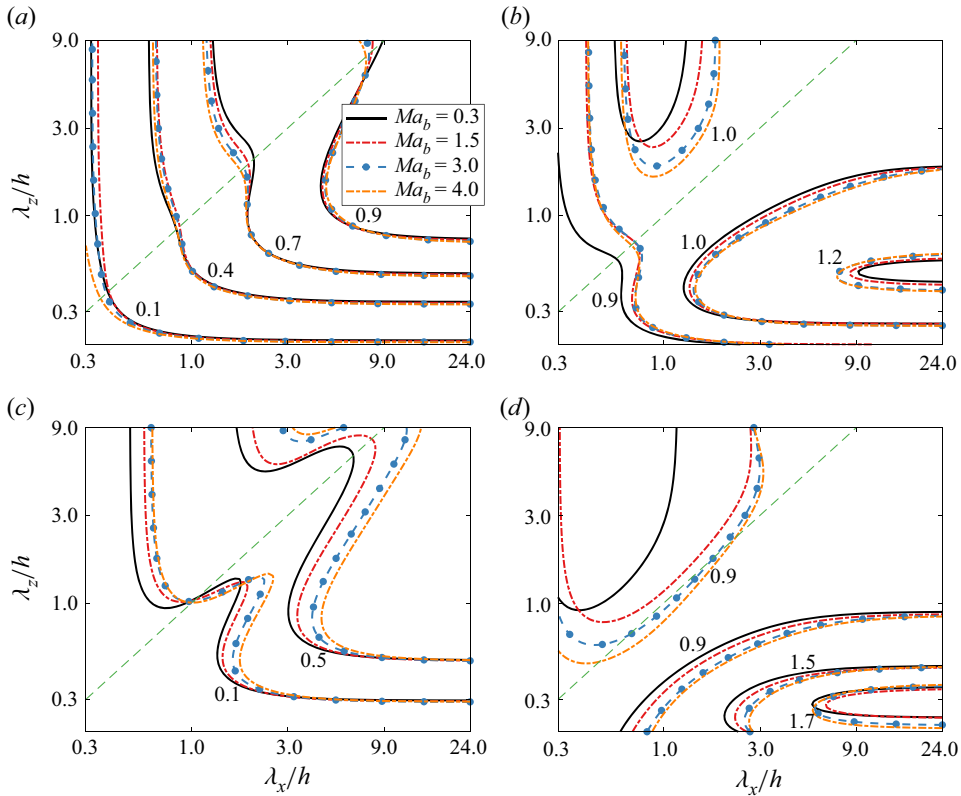
Figure 22. Contours of (*a*,*c*) γ_{uu}^2 and (*b*,*d*) $A_{pm,uu}$ in the cases of varying Ma_b but the same $Re_{\tau,c}^*$. Here, y_m^* is fixed at 107, and (*a*,*b*) $y_p^* = 70$ and (*c*,*d*) $y_p^* = 10$. The levels are labelled in the figures. The green dotted lines denote $\lambda_x = \lambda_z$.

above concerning the effects of acoustic and entropy modes on temperature are limited to the case of $Ma_b = 1.5$, awaiting future examination at higher Ma_b using the DNS data.

7. Discussions

7.1. *Other linear models with turbulence modelling*

As introduced in § 3.2, there are a number of combinations of turbulence modelling relations to linearize the fluctuation equations, leading to different linear models. Since (3.6) is used, they can all be considered as eddy viscosity enhanced ones, so for ease of writing, the eLNS model presented above using (3.10*a*,*b*) is termed the benchmark eLNS model. We have examined other eLNS models, including

(i) using (3.8*b*) instead of (3.8*a*) to linearize the turbulent heat flux;
(ii) adding k'' as an independent variable (so six equations with the basic variable set $q'' = [\rho', u'', v'', w'', T'', k'']^T$) to linearize the dissipation rate and the k'' equation;
(iii) linearizing ρ' (in N_ρ'', N_{u_i}'' and N_T'') using the SRA in (3.16*a*,*b*) (similar to (3.8)).

They are termed the adjusted eLNS models collectively. Same as the benchmark eLNS model, non-negligible contributions of acoustic and entropy components to $\boldsymbol{\Phi}$ are all present in these adjusted models, because the eigenmodes are damped by μ_t and the non-normality of the linear operator (in particular, the vortical mode branch) decreases as in § 4. Consequently, the SLSE results from these adjusted models are all largely

973 A36-37

different from DNS regarding the temperature fluctuations, similar to the benchmark eLNS model (see § 5.3). Thereby, detailed comparisons among these eLNS models are not provided considering the collective failure, and the main focus has been paid to the mathematical features of the linear model for possible explanations of the deviation, as has been elaborated in §§ 4 and 5.4. The procedure of cospectrum decomposition is thus introduced to obtain basically agreeable results with the DNS data.

7.2. *Implications for calculating boundary layer flows*

As shown in figure 13, there are a series of acoustic modes in the POD of $\boldsymbol{\Phi}$ with different k_y, oscillating in the outer region. Bounded by the two walls at $y = 0$ and $2h$ in the channel flow, k_y is discretized so only those with $\lambda_y = 2h/n$ are allowed (n is an integer). In analogy, the acoustic modes exist in boundary layer flows, and their k_y are determined by the height of the computational domain. Different from the channel flow, the location of the upper boundary is in the free stream and is artificially selected in the boundary layers, so the results of the acoustic modes and thus $\boldsymbol{\Phi}$ can be dependent on the domain height, which seems not physically appropriate. When the response mode is relatively supersonic (phase speed ω/k_x larger than the free stream acoustic wave, either downstream or upstream), the acoustic components in the free stream are highly pronounced, so the responses from input–output or resolvent analyses can be tightly dependent on the computational domain, as noted by Bae *et al.* (2020) and Madhusudanan & McKeon (2022). The present work suggests that such a prominent role of acoustic modes in the linear models is not in line with DNS, within at least the *Ma* considered. As one solution candidate, the cospectrum decomposition procedure can be used to identify and remove the acoustic components. Detailed comparisons with experimental or DNS data for boundary layer flows are anticipated to assess further the behaviour of the linear models in different configurations.

7.3. *Implications for the turbulence modelling simulations*

The discussions in § 4 concerning $\hat{\mathcal{L}}_{eLNS}$ and μ_t in compressible flows may be of greater significance in some RANS-related applications. The linear operator can be encountered, e.g. in the sensitivity analysis of RANS modelling to field variables, and in some spatial numerical schemes in the computational fluid dynamics where linearization of the inviscid and viscous fluxes towards basic variables is required (see e.g. MacCormack 1985). Also, the linear operator can, at least partially, govern the transient dynamics when the turbulent flow is perturbed around its statistically equilibrium state, simulated using, e.g. unsteady RANS simulations, detached eddy simulations or wall-modelled large eddy simulations. The diminishing non-normality of the linear operator due to μ_t can overdamp the vortical modes, hence leading to possibly overemphasized roles of the acoustic and entropy modes. Nevertheless, this effect can be difficult to isolate due to the combined complexities of flow physics (shocks, separation, etc.), more sophisticated turbulence models, numerical schemes, grid resolutions and so on. More future explorations are anticipated in this direction.

8. Summary

In this work, the linear models, based on stochastically forced linearized NS equations, are deployed for SLSE of the velocity and temperature fluctuations in compressible turbulent channel flows. The benchmark case has $Ma_b = 1.5$ and $Re_b = 20\,020$. The spectral coherence and amplitude ratio (γ^2 and A_{pm}) of the fluctuation between

different wall-normal heights are obtained using the linear models with only mean flow input. Afterwards, the coherent portion of the instantaneous field at other heights can be estimated through H_L based on one snapshot at the measurement height. Three aspects are mainly focused on, namely the derivation and mathematical features of the linear models, quantitative comparison of the SLSE quantities with the DNS data, and the structural coherence of velocity and temperature fluctuations inferred by the SLSE results.

First, the derivation of the linear model is discussed carefully. The full expressions of the fluctuation equations are provided, and the assumptions for linearization are detailed. Two types of models are considered. The first is the LNS model with all the nonlinear terms collected into the forcing term, while the second is the eddy viscosity enhanced one (eLNS model), using turbulence modelling relations for possible linearization of the nonlinear terms. The mathematical properties of the linear operator are scrutinized by studying their eigenspectra and pseudospectra. There are four branches of eigenmodes for $\hat{\mathcal{L}}_{LNS}$ and $\hat{\mathcal{L}}_{eLNS}$, and the vortical branch has strong non-normality to support the transient behaviour of the fluctuations. For the LNS model, the acoustic modes have little non-normality and increasingly small contributions to the energy growth as length scales (both λ_x and λ_z) increase. In contrast, the non-normality of the vortical modes diminishes in the eLNS model, closely related to the damping effects of μ_t (and κ_t) on the eigenmodes. Consequently, the acoustic and entropy modes can account for 20 % to 55 % of the response energy growth, which largely affects the SLSE results for temperature.

The SLSE results (γ^2, A_{pm} and H_L) for streamwise velocity are quite similar to the incompressible case. The eLNS model outperforms the LNS model, giving basically agreeable results with the DNS data, though the structures of small λ_z are still somewhat underestimated. However, both models have considerable deviations from DNS regarding temperature and velocity–temperature coupling. A decomposition of the eLNS cospectrum ($\boldsymbol{\Phi}_{nae}$ and $\boldsymbol{\Phi}_{ae}$) shows that the acoustic and entropy components hardly affect the streamwise-velocity cospectrum, but have non-negligible contributions (especially the acoustic ones) to those of density and temperature, which is not supported by the DNS data. Thereby, the prominent role of acoustic and entropy components for the response growth is an intrinsic defect of the eLNS model introduced by the turbulence modelling related to μ_t. A procedure of cospectrum decomposition is thus designed to remove the acoustic and entropy components (eLNS-CD). The resulting SLSE quantities for temperature and velocity–temperature coupling show a noticeable improvement over the eLNS model, and are basically agreeable with DNS, except in the region of small λ_x. Thereby, the coherent velocity and temperature fluctuations are dominated by advection and other vortical motions, while the compressibility effects are of secondary importance.

Finally, a parameter study is conducted for four cases with varying Ma_b (0.3–4) but the same $Re_{\tau,c}^*$. Semi-local units well collapse γ_{uu}^2 and $A_{pm,uu}$ to the incompressible case for the streamwise-elongated structures of high coherence, which benefits the modelling of inner–outer interaction for compressible flows. In contrast, the spanwise-elongated structures ($\lambda_x < \lambda_z$) are more influenced by Ma_b. Moreover, the behaviours of other linear models with different turbulence modelling relations are discussed. Some implications are presented for calculating the boundary layer flows and dealing with RANS-related computations.

Future works will be focused on assessing the behaviours of the linear models for compressible cases at higher Ma_b and Re and incompressible cases with heat transfer, using the DNS or experimental data. Improvements on the linear models are anticipated

through, e.g. modified linearization of turbulent eddy terms and more realistic modelling of the forcing.

Declaration of interests. The authors report no conflict of interest.

Data availability statement. The data that support the findings of this study are available from the corresponding author upon reasonable request.

Author ORCIDs.

- Xianliang Chen https://orcid.org/0000-0002-7540-3395;
- Cheng Cheng https://orcid.org/0000-0002-7961-793X;
- Jianping Gan https://orcid.org/0000-0001-9827-7929;
- Lin Fu https://orcid.org/0000-0001-8979-8415.

Appendix A. Fluctuation equation for turbulent kinetic energy

Based on (3.3), the equation for k'' is derived as

$$
\bar{\rho}\left(\frac{\partial k''}{\partial t} + \tilde{u}_j\frac{\partial k''}{\partial x_j}\right) + \rho'\frac{\partial k}{\partial t} + (\rho'\tilde{u}_j + \bar{\rho}u_j'')\frac{\partial k}{\partial x_j}
$$

$$
= -\bar{\rho}(u_i''u_j'' - \widetilde{u_i''u_j''})\frac{\partial \tilde{u}_i}{\partial x_j} - \bar{\rho}\widetilde{u_i''u_j''}\frac{\partial u_i''}{\partial x_j}
$$

$$
- \frac{\partial}{\partial x_j}[\bar{\rho}(u_j''k'' - \widetilde{u_j''k''} - u_i''\widetilde{u_i''u_j''})] - \left(\frac{\partial p'u_j''}{\partial x_j} - \frac{\partial \overline{p'u_j''}}{\partial x_j}\right)
$$

$$
+ \left(p'\frac{\partial u_j''}{\partial x_j} - \overline{p'\frac{\partial u_j''}{\partial x_j}}\right) + \left(\frac{\partial \tau_{ij}'u_i''}{\partial x_j} - \frac{\partial \overline{\tau_{ij}'u_i''}}{\partial x_j}\right) - \left(\tau_{ij}'\frac{\partial u_i''}{\partial x_j} - \overline{\tau_{ij}'\frac{\partial u_i''}{\partial x_j}}\right)
$$

$$
- \left[\frac{\partial \rho'k''}{\partial t} + \frac{\partial \rho'(\tilde{u}_j + u_j'')k''}{\partial x_j} + \rho'u_j''\frac{\partial k}{\partial x_j} + \rho'u_i''\left(\frac{\partial \tilde{u}_i}{\partial t} + (\tilde{u}_j + u_j'')\frac{\partial \tilde{u}_i}{\partial x_j}\right)\right]. \quad (A1)
$$

As in (3.4*c*), there are fluctuations of turbulent heat flux, pressure dilatation and dissipation rate, so these terms are responsible for the energy transfer between $c_v T''$ and k''. The first two terms on the right-hand side are the fluctuating turbulent production term, which can be linearized using (3.6). The resulting term takes the same form as the linearized viscous dissipation term (the last term on the left-hand side in (3.4*c*)) except for replacing $\tilde{\mu}$ with μ_t. Equation (A1) can be included in (3.4) to solve the problem in § 3.3 if k'' is treated as the sixth independent variable, as discussed in § 7.1.

Appendix B. Eigenmodes in inviscid uniform mean flow

An inviscid uniform mean flow (using the channel-centre value, $\tilde{\mu} = \mu_t = 0$) is considered. Since there are no wall-normal gradients of the mean flow, the fluctuation is assumed to be periodic in the wall-normal direction with a wavenumber k_y (see (2.3)).

The linear operator $\hat{\mathcal{L}}_c$ then takes the form of

$$
\hat{\mathcal{L}}_c = \begin{bmatrix}
\mathrm{i}k_x\tilde{u}_c & \mathrm{i}k_x\bar{\rho} & \mathrm{i}k_y\bar{\rho} & \mathrm{i}k_z\bar{\rho} & 0 \\
\mathrm{i}k_x R\dfrac{\tilde{T}_c}{\bar{\rho}_c} & \mathrm{i}k_x\tilde{u}_c & 0 & 0 & \mathrm{i}k_x R \\
\mathrm{i}k_y R\dfrac{\tilde{T}_c}{\bar{\rho}_c} & 0 & \mathrm{i}k_x\tilde{u}_c & 0 & \mathrm{i}k_y R \\
\mathrm{i}k_z R\dfrac{\tilde{T}_c}{\bar{\rho}_c} & 0 & 0 & \mathrm{i}k_x\tilde{u}_c & \mathrm{i}k_z R \\
0 & \mathrm{i}k_x(\gamma_0 - 1)\tilde{T}_c & \mathrm{i}k_y(\gamma_0 - 1)\tilde{T}_c & \mathrm{i}k_z(\gamma_0 - 1)\tilde{T}_c & \mathrm{i}k_x\tilde{u}_c
\end{bmatrix}. \tag{B1}
$$

After applying the energy norm, the five eigenvalues of $\hat{\mathcal{L}}_c$ are obtained, as shown in (4.1). The orthogonal eigenfunctions (along with the linearized pressure and entropy fluctuations) $\check{q} = [\check{\rho}', \check{u}'', \check{v}'', \check{w}'', \check{T}'', \check{p}', \check{s}'']^{\mathrm{T}}$ are specified below.

Fast and slow acoustic modes:

$$
\check{q} = \frac{1}{\sqrt{2\gamma_0\bar{p}}}\left[\pm\bar{\rho}, \ \frac{k_x}{\check{k}}a, \ \frac{k_y}{\check{k}}a, \ \frac{k_z}{\check{k}}a, \ \pm(\gamma_0 - 1)\tilde{T}, \pm\gamma_0\bar{p}, \ 0\right]^{\mathrm{T}}, \tag{B2a}
$$

Entropy mode:

$$
\check{q} = \frac{\sqrt{\gamma_0 - 1}}{\sqrt{\gamma_0\bar{p}}}[\bar{\rho}, \ 0, \ 0, \ 0, \ -\tilde{T}, \ 0, \ -\gamma_0\bar{s}]^{\mathrm{T}}, \tag{B2b}
$$

Vortical mode:

$$
\check{q} = \frac{1}{\sqrt{\gamma_0\bar{p}}}[0, \ t_{ix}a, \ t_{iy}a, \ t_{iz}a, \ 0, \ 0, \ 0]^{\mathrm{T}}, \quad i = 1, 2. \tag{B2c}
$$

Here, $\check{k}^2$ equals $k_x^2 + k_y^2 + k_z^2$ (notation $\check{k}$ distinguished from the turbulent kinetic energy k), and $[t_{ix}, t_{iy}, t_{iz}]^{\mathrm{T}}$ ($i = 1, 2$) are two unit vectors perpendicular to $[k_x, k_y, k_z]^{\mathrm{T}}$. The mean entropy is $\bar{s} = \bar{p}/\bar{\rho}^{\gamma_0}$. Different modes in (B2) are perpendicular to each other in terms of (3.13) (George & Sujith 2011), so $\hat{\mathcal{L}}_c$ is normal. To classify different modes in the channel flows (see §§ 4.2 and 5.4), the eigenfunction is normalized first, to be applicable to flows of different Ma_b, as $\check{q}_{nrm} = [\check{\rho}'/\bar{\rho}, \check{u}''/a, \check{v}''/a, \check{w}''/a, \check{T}''/\tilde{T}, \check{p}'/\bar{p}]^{\mathrm{T}}$. Afterwards, (B2) is used to judge whether the pressure, kinematic or thermodynamic component has the largest amplitude (see figure 4).

Appendix C. Growth-rate decomposition for eigenmodes

The growth-rate decomposition can quantify the contributions of each term in the governing equation to the eigenmode growth rates (see e.g. Chen, Wang & Fu (2022a) and Chen *et al.* (2022b) for more detail). Hence the growth-rate difference between the LNS and eLNS eigenmodes can be explained. The decomposition is realized after left-multiplying $\hat{q}''^H M$ to (3.12) and adding the complex conjugate. Note that $\hat{f}$ is not considered for the eigenmodes. The classified terms are defined as follows. The production is sum of the terms related to $\check{v}''$ and the mean flow gradients ($\partial\tilde{u}/\partial y$, $\partial\bar{\rho}/\partial y$ and $\partial\tilde{T}/\partial y$). The pressure dilatation is $\check{p}\nabla \cdot \check{u}$ and the pressure work is $\check{u} \cdot \nabla\check{p}$. The viscous and diffusive terms are those related to $\tilde{\mu}$ and $\tilde{\kappa}$, and the eddy viscous and diffusive terms are those related to μ_t and κ_t. The decomposition results for the least stable three types of eigenmodes are listed in table 2 (see their shapes in figure 4). The difference in ω_i

Modes	Prod.	PreD.	PreW.	VsDf.	EVsDf.	sum (ω_i)
Acoustic, LNS	0.0024	−0.0003	0.0003	−0.0085	0.0000	−0.0061
Acoustic, eLNS	0.0024	−0.0072	0.0072	−0.0083	−0.0324	−0.0383
Vortical, LNS	0.0000	0.0000	0.0000	−0.0039	0.0000	−0.0039
Vortical, eLNS	−0.0001	0.0000	0.0000	−0.0011	−0.0581	−0.0593
Entropy, LNS	0.0000	0.0000	0.0000	−0.0048	0.0000	−0.0048
Entropy, eLNS	0.0000	0.0000	0.0000	−0.0016	−0.0734	−0.0750

Table 2. Growth-rate decomposition for the least stable eigenmodes of the LNS and eLNS linear operators (shapes in figure 4, $\lambda_x = 8h$, $\lambda_z = 2h$). The results are non-dimensionalized by U_b/h. Term abbreviations: Prod. for production; PreD. for pressure dilatation; PreW. for pressure work; VsDf. for viscosity and diffusivity; EVsDf. for eddy viscosity and diffusivity.

between the LNS and eLNS eigenmodes is mainly caused by the eddy terms, the same for the acoustic, vortical and entropy branches. Thereby, the conclusion in § 4.1 is supported that the eddy terms related to μ_t and κ_t severely stabilize the eigenmodes.

REFERENCES

ABE, H. & ANTONIA, R.A. 2017 Relationship between the heat transfer law and the scalar dissipation function in a turbulent channel flow. *J. Fluid Mech.* **830**, 300–325.

ABE, H., ANTONIA, R.A. & TOH, S. 2018 Large-scale structures in a turbulent channel flow with a minimal streamwise flow unit. *J. Fluid Mech.* **850**, 733–768.

ABE, H., KAWAMURA, H. & CHOI, H. 2004 Very large-scale structures and their effects on the wall shear-stress fluctuations in a turbulent channel flow up to $Re_\tau = 640$. *Trans. ASME J. Fluids Engng* **126** (5), 835–843.

ADRIAN, R.J. 1979 Conditional eddies in isotropic turbulence. *Phys. Fluids* **22** (11), 2065–2070.

ADRIAN, R.J. & MOIN, P. 1988 Stochastic estimation of organized turbulent structure: homogeneous shear flow. *J. Fluid Mech.* **190**, 531–559.

AGOSTINI, L. & LESCHZINER, M.A. 2014 On the influence of outer large-scale structures on near-wall turbulence in channel flow. *Phys. Fluids* **26** (7), 075107.

DEL ÁLAMO, J.C. & JIMÉNEZ, J. 2006 Linear energy amplification in turbulent channels. *J. Fluid Mech.* **559**, 205–213.

ALIZARD, F., GIBIS, T., SELENT, B., RIST, U. & WENZEL, C. 2022 Stochastic receptivity of laminar compressible boundary layers: an input-output analysis. *Phys. Rev. Fluids* **7** (7), 073902.

ALIZARD, F., PIROZZOLI, S., BERNARDINI, M. & GRASSO, F. 2015 Optimal transient growth in compressible turbulent boundary layers. *J. Fluid Mech.* **770**, 124–155.

ANTONIA, R.A., ABE, H. & KAWAMURA, H. 2009 Analogy between velocity and scalar fields in a turbulent channel flow. *J. Fluid Mech.* **628**, 241–268.

BAARS, W.J., HUTCHINS, N. & MARUSIC, I. 2016 Spectral stochastic estimation of high-Reynolds-number wall-bounded turbulence for a refined inner-outer interaction model. *Phys. Rev. Fluids* **1** (5), 054406.

BAARS, W.J., HUTCHINS, N. & MARUSIC, I. 2017 Self-similarity of wall-attached turbulence in boundary layers. *J. Fluid Mech.* **823**, R2.

BAE, H.J., DAWSON, S.T.M. & MCKEON, B.J. 2020 Resolvent-based study of compressibility effects on supersonic turbulent boundary layers. *J. Fluid Mech.* **883**, A29.

BAI, T., CHENG, C. & FU, L. 2023 Effects of mean shear on the vortex identification and the orientation statistics. *Theor. Appl. Mech. Lett.* **13** (1), 100454.

BAI, T., GRIFFIN, K.P. & FU, L. 2022 Compressible velocity transformations for various noncanonical wall-bounded turbulent flows. *AIAA J.* **60** (7), 4325–4337.

BALAKUMAR, P. & MALIK, M.R. 1992 Discrete modes and continuous spectra in supersonic boundary layers. *J. Fluid Mech.* **239**, 631–656.

BERNARDINI, M. & PIROZZOLI, S. 2011 Inner/outer layer interactions in turbulent boundary layers: a refined measure for the large-scale amplitude modulation mechanism. *Phys. Fluids* **23** (6), 061701.

BRADSHAW, P. 1977 Compressible turbulent shear layers. *Annu. Rev. Fluid Mech.* **9** (1), 33–52.

BROSS, M., SCHARNOWSKI, S. & KÄHLER, C.J. 2021 Large-scale coherent structures in compressible turbulent boundary layers. *J. Fluid Mech.* **911**, A2.

CHEN, X., CHENG, C., FU, L. & GAN, J. 2023 Linear response analysis of supersonic turbulent channel flows with a large parameter space. *J. Fluid Mech.* **962**, A7.

CHEN, X., WANG, L. & FU, S. 2022*a* Energy transfer of hypersonic and high-enthalpy boundary layer instabilities and transition. *Phys. Rev. Fluids* **7** (3), 033901.

CHEN, X., XI, Y., REN, J. & FU, S. 2022*b* Cross-flow vortices and their secondary instabilities in hypersonic and high-enthalpy boundary layers. *J. Fluid Mech.* **947**, A25.

CHENG, C. & FU, L. 2022*a* Consistency between the attached-eddy model and the inner-outer interaction model: a study of streamwise wall-shear stress fluctuations in a turbulent channel flow. *J. Fluid Mech.* **942**, R9.

CHENG, C. & FU, L. 2022*b* Large-scale motions and self-similar structures in compressible turbulent channel flows. *Phys. Rev. Fluids* **7** (11), 114604.

CHENG, C. & FU, L. 2023*a* Linear-model-based study of the coupling between velocity and temperature fields in compressible turbulent channel flows. *J. Fluid Mech.* **964**, A15.

CHENG, C. & FU, L. 2023*b* A scale-based study of the Reynolds number scaling for the near-wall streamwise turbulence intensity in wall turbulence. *Intl J. Heat Fluid Flow* **101**, 109136.

CHENG, C., SHYY, W. & FU, L. 2022 Streamwise inclination angle of wall-attached eddies in turbulent channel flows. *J. Fluid Mech.* **946**, A49.

CHOMAZ, J.-M. 2005 Global instabilities in spatially developing flows: non-normality and nonlinearity. *Annu. Rev. Fluid Mech.* **37** (1), 357–392.

CHU, B.-T. 1965 On the energy transfer to small disturbances in fluid flow (part I). *Acta Mech.* **1** (3), 215–234.

COGO, M., SALVADORE, F., PICANO, F. & BERNARDINI, M. 2022 Direct numerical simulation of supersonic and hypersonic turbulent boundary layers at moderate-high Reynolds numbers and isothermal wall condition. *J. Fluid Mech.* **945**, A30.

COLEMAN, G.N., KIM, J. & MOSER, R.D. 1995 A numerical study of turbulent supersonic isothermal-wall channel flow. *J. Fluid Mech.* **305**, 159–183.

DAWSON, S.T.M. & MCKEON, B.J. 2020 Prediction of resolvent mode shapes in supersonic turbulent boundary layers. *Intl J. Heat Fluid Flow* **85**, 108677.

DI RENZO, M., FU, L. & URZAY, J. 2020 HTR solver: an open-source exascale-oriented task-based multi-GPU high-order code for hypersonic aerothermodynamics. *Comput. Phys. Commun.* **255**, 107262.

DI RENZO, M. & URZAY, J. 2021 Direct numerical simulation of a hypersonic transitional boundary layer at suborbital enthalpies. *J. Fluid Mech.* **912**, A29.

VAN DRIEST, E.R. 1951 Turbulent boundary layer in compressible fluids. *J. Aeronaut. Sci.* **18** (3), 145–160.

DUAN, L., BEEKMAN, I. & MARTIN, M.P. 2010 Direct numerical simulation of hypersonic turbulent boundary layers. Part 2. Effect of wall temperature. *J. Fluid Mech.* **655**, 419–445.

DUAN, L. & MARTÍN, M.P. 2011 Direct numerical simulation of hypersonic turbulent boundary layers. Part 4. Effect of high enthalpy. *J. Fluid Mech.* **684**, 25–59.

ENCINAR, M.P. & JIMÉNEZ, J. 2019 Logarithmic-layer turbulence: a view from the wall. *Phys. Rev. Fluids* **4** (11), 114603.

FARRELL, B.F. & IOANNOU, P.J. 1993 Stochastic forcing of the linearized Navier–Stokes equations. *Phys. Fluids* A*: Fluid Dyn.* **5** (11), 2600–2609.

FOYSI, H., SARKAR, S. & FRIEDRICH, R. 2004 Compressibility effects and turbulence scalings in supersonic channel flow. *J. Fluid Mech.* **509**, 207–216.

FU, L., BOSE, S. & MOIN, P. 2022 Prediction of aerothermal characteristics of a generic hypersonic inlet flow. *Theor. Comput. Fluid Dyn.* **36** (2), 345–368.

FU, L., KARP, M., BOSE, S.T., MOIN, P. & URZAY, J. 2021 Shock-induced heating and transition to turbulence in a hypersonic boundary layer. *J. Fluid Mech.* **909**, A8.

GANAPATHISUBRAMANI, B., CLEMENS, N.T. & DOLLING, D.S. 2006 Large-scale motions in a supersonic turbulent boundary layer. *J. Fluid Mech.* **556**, 271–282.

GATSKI, T.B. & BONNET, J.-P. 2013 *Compressibility, Turbulence and High Speed Flow*, 2nd edn. Academic.

GEORGE, K.J. & SUJITH, R.I. 2011 On Chu's disturbance energy. *J. Sound Vib.* **330** (22), 5280–5291.

GRIFFIN, K.P., FU, L. & MOIN, P. 2021 Velocity transformation for compressible wall-bounded turbulent flows with and without heat transfer. *Proc. Natl Acad. Sci.* **118** (34), e2111144118.

GRIFFIN, K., FU, L. & MOIN, P. 2022 *Wall Model for Large-Eddy Simulation of Compressible Turbulent Flows*. Bulletin of the American Physical Society.

GRIFFIN, K.P., FU, L. & MOIN, P. 2023 Near-wall model for compressible turbulent boundary layers based on an inverse velocity transformation. *J. Fluid Mech.* **970**, A36.

GUPTA, V., MADHUSUDANAN, A., WAN, M., ILLINGWORTH, S.J. & JUNIPER, M.P. 2021 Linear-model-based estimation in wall turbulence: improved stochastic forcing and eddy viscosity terms. *J. Fluid Mech.* **925**, A18.

HAMILTON, J.M., KIM, J. & WALEFFE, F. 1995 Regeneration mechanisms of near-wall turbulence structures. *J. Fluid Mech.* **287**, 317–348.

HANIFI, A., SCHMID, P.J. & HENNINGSON, D.S. 1996 Transient growth in compressible boundary layer flow. *Phys. Fluids* **8** (3), 826–837.

HUANG, P.G., COLEMAN, G.N. & BRADSHAW, P. 1995 Compressible turbulent channel flows: DNS results and modelling. *J. Fluid Mech.* **305**, 185–218.

HUANG, J., DUAN, L. & CHOUDHARI, M.M. 2022 Direct numerical simulation of hypersonic turbulent boundary layers: effect of spatial evolution and Reynolds number. *J. Fluid Mech.* **937**, A3.

HUTCHINS, N. & MARUSIC, I. 2007 Evidence of very long meandering features in the logarithmic region of turbulent boundary layers. *J. Fluid Mech.* **579**, 1–28.

HWANG, Y. & COSSU, C. 2010 Linear non-normal energy amplification of harmonic and stochastic forcing in the turbulent channel flow. *J. Fluid Mech.* **664**, 51–73.

ILLINGWORTH, S.J., MONTY, J.P. & MARUSIC, I. 2018 Estimating large-scale structures in wall turbulence using linear models. *J. Fluid Mech.* **842**, 146–162.

JONES, W.P. & LAUNDER, B.E. 1972 The prediction of laminarization with a two-equation model of turbulence. *Intl J. Heat Mass Transfer* **15** (2), 301–314.

KIM, K.C. & ADRIAN, R.J. 1999 Very large-scale motion in the outer layer. *Phys. Fluids* **11** (2), 417–422.

KUHN, P., MÜLLER, J.S., KNECHTEL, S., SORIA, J. & OBERLEITHNER, K. 2022 Influence of eddy viscosity on linear modeling of self-similar coherent structures in the jet far field. In *AIAA SCITECH 2022 Forum*. American Institute of Aeronautics and Astronautics.

LAGHA, M., KIM, J., ELDREDGE, J.D. & ZHONG, X. 2011 A numerical study of compressible turbulent boundary layers. *Phys. Fluids* **23** (1), 015106.

LELE, S.K. 1994 Compressibility effects on turbulence. *Annu. Rev. Fluid Mech.* **26** (1), 211–254.

MACCORMACK, R. 1985 Current status of numerical solutions of the Navier–Stokes equations. In *23rd Aerospace Sciences Meeting*. American Institute of Aeronautics and Astronautics.

MACK, L.M. 1984 Boundary-layer linear stability theory. *Tech. Rep.* 709. AGARD Special Course on Stability and Transition of Laminar Flow.

MADHUSUDANAN, A., ILLINGWORTH, S.J. & MARUSIC, I. 2019 Coherent large-scale structures from the linearized Navier–Stokes equations. *J. Fluid Mech.* **873**, 89–109.

MADHUSUDANAN, A. & MCKEON, B.J. 2022 Subsonic and supersonic mechanisms in compressible turbulent boundary layers: a perspective from resolvent analysis. Preprint, arXiv:2209.14223.

MALKUS, W.V.R. 1956 Outline of a theory of turbulent shear flow. *J. Fluid Mech.* **1** (5), 521–539.

MARUSIC, I., MATHIS, R. & HUTCHINS, N. 2010 Predictive model for wall-bounded turbulent flow. *Science* **329** (5988), 193–196.

MCKEON, B.J. 2019 Self-similar hierarchies and attached eddies. *Phys. Rev. Fluids* **4** (8), 082601.

MCKEON, B.J. & SHARMA, A.S. 2010 A critical-layer framework for turbulent pipe flow. *J. Fluid Mech.* **658**, 336–382.

MOARREF, R. & JOVANOVIĆ, M.R. 2012 Model-based design of transverse wall oscillations for turbulent drag reduction. *J. Fluid Mech.* **707**, 205–240.

MOARREF, R., SHARMA, A.S., TROPP, J.A. & MCKEON, B.J. 2013 Model-based scaling of the streamwise energy density in high-Reynolds-number turbulent channels. *J. Fluid Mech.* **734**, 275–316.

MOIN, P. & MAHESH, K. 1998 Direct numerical simulation: a tool in turbulence research. *Annu. Rev. Fluid Mech.* **30**, 539–578.

MORINISHI, Y., TAMANO, S. & NAKABAYASHI, K. 2004 Direct numerical simulation of compressible turbulent channel flow between adiabatic and isothermal walls. *J. Fluid Mech.* **502**, 273–308.

MORKOVIN, M.V. 1962 Effects of compressibility on turbulent flows. In *Mécanique de la Turbulence* (ed. A. Favre), pp.367–380. CNRS.

MORRA, P., NOGUEIRA, P.A.S., CAVALIERI, A.V.G. & HENNINGSON, D.S. 2021 The colour of forcing statistics in resolvent analyses of turbulent channel flows. *J. Fluid Mech.* **907**, A24.

PICKERING, E.M., RIGAS, G., SCHMIDT, O.T., SIPP, D. & COLONIUS, T. 2021 Optimal eddy viscosity for resolvent-based models of coherent structures in turbulent jets. *J. Fluid Mech.* **917**, A29.

PIROZZOLI, S. & BERNARDINI, M. 2011 Turbulence in supersonic boundary layers at moderate Reynolds number. *J. Fluid Mech.* **688**, 120–168.

PIROZZOLI, S., BERNARDINI, M. & GRASSO, F. 2008 Characterization of coherent vortical structures in a supersonic turbulent boundary layer. *J. Fluid Mech.* **613**, 205–231.

PIROZZOLI, S., GRASSO, F. & GATSKI, T.B. 2004 Direct numerical simulation and analysis of a spatially evolving supersonic turbulent boundary layer at $M = 2.25$. *Phys. Fluids* **16** (3), 530–545.

RAN, W., ZARE, A. & JOVANOVIĆ, M.R. 2020 Model-based design of riblets for turbulent drag reduction. *J. Fluid Mech.* **906**, A7.

REYNOLDS, W.C. & HUSSAIN, A.K.M.F. 1972 The mechanics of an organized wave in turbulent shear flow. Part 3. Theoretical models and comparisons with experiments. *J. Fluid Mech.* **54** (2), 263–288.

RINGUETTE, M.J., WU, M. & MARTÍN, M.P. 2008 Coherent structures in direct numerical simulation of turbulent boundary layers at Mach 3. *J. Fluid Mech.* **594**, 59–69.

SCHMID, P.J. & HENNINGSON, D.S. 2001 *Stability and Transition in Shear Flows*. Springer.

SCHOPPA, W. & HUSSAIN, F. 2002 Coherent structure generation in near-wall turbulence. *J. Fluid Mech.* **453**, 57–108.

SMITH, M.W. & SMITS, A.J. 1995 Visualization of the structure of supersonic turbulent boundary layers. *Exp. Fluids* **18** (4), 288–302.

SONG, Y., ZHANG, P. & XIA, Z. 2023 Predicting mean profiles in compressible turbulent channel and pipe flows. *Phys. Rev. Fluids* **8** (3), 034604.

SYMON, S., ILLINGWORTH, S.J. & MARUSIC, I. 2021 Energy transfer in turbulent channel flows and implications for resolvent modelling. *J. Fluid Mech.* **911**, A3.

TINNEY, C.E., COIFFET, F., DELVILLE, J., HALL, A.M., JORDAN, P. & GLAUSER, M.N. 2006 On spectral linear stochastic estimation. *Exp. Fluids* **41** (5), 763–775.

TOWNSEND, A.A.R. 1976 *The Structure of Turbulent Shear Flow*, 2nd edn. Cambridge University Press.

TREFETHEN, L.N. 1997 Pseudospectra of linear operators. *SIAM Rev.* **39** (3), 383–406.

TREFETHEN, L.N., TREFETHEN, A.E., REDDY, S.C. & DRISCOLL, T.A. 1993 Hydrodynamic stability without eigenvalues. *Science* **261** (5121), 578–584.

TRETTEL, A. & LARSSON, J. 2016 Mean velocity scaling for compressible wall turbulence with heat transfer. *Phys. Fluids* **28** (2), 026102.

WALZ, A. 1969 *Boundary Layers of Flow and Temperature*. MIT Press.

WILCOX, D.C. 2006 *Turbulence Modeling for CFD*, 3rd edn. DCW Industries.

WILLIAMS, O.J.H., SAHOO, D., BAUMGARTNER, M.L. & SMITS, A.J. 2018 Experiments on the structure and scaling of hypersonic turbulent boundary layers. *J. Fluid Mech.* **834**, 237–270.

YAO, J. & HUSSAIN, F. 2020 Turbulence statistics and coherent structures in compressible channel flow. *Phys. Rev. Fluids* **5** (8), 084603.

YU, M. & XU, C. 2022 Predictive models for near-wall velocity and temperature fluctuations in supersonic wall-bounded turbulence. *J. Fluid Mech.* **937**, A32.

YU, M., XU, C., CHEN, J., LIU, P., FU, Y. & YUAN, X. 2022 Spectral decomposition of wall-attached/detached eddies in compressible and incompressible turbulent channel flows. *Phys. Rev. Fluids* **7** (5), 054607.

ZHANG, Y.-S., BI, W.-T., HUSSAIN, F. & SHE, Z.-S. 2014 A generalized Reynolds analogy for compressible wall-bounded turbulent flows. *J. Fluid Mech.* **739**, 392–420.